

FREEZE DRIED POWDER OF SELECTED THAI UPLAND-RICE GRASS JUICE

PHEAKDEY YUN

**A THESIS SUBMITTED IN PARTIAL FULFILLMENT
OF THE REQUIREMENT FOR THE DEGREE OF
MASTER OF SCIENCE IN FOOD SCIENCE
FACULTY OF AGRO-INDUSTRY
KING MONGKUT'S INSTITUTE OF TECHNOLOGY LADKRAEANG**

2016

KMITL-2016-AI-M-058-251

OPTICAL PHENOMENA IN NESTED MICRORING RESONATOR



RANGSAN JOMTARAK

เลขหมู่.....
เลขทะเบียน 077661
วันเดือนปี 1 ส.ค. 2559

.b.....
.i.....

A THESIS SUBMITTED IN FULFILLMENT OF THE REQUIREMENT FOR THE
DEGREE OF DOCTOR OF PHILOSOPHY IN APPLIED PHYSICS

FACULTY OF SCIENCE

KING MONGKUT'S INSTITUTE OF TECHNOLOGY LADKRABANG

2015

KMITL-2015-SC-D-030-064

COPYRIGHT 2015

FACULTY OF SCIENCE

KING MONGKUT'S INSTITUTE OF TECHNOLOGY LADKRABANG

หัวข้อวิทยานิพนธ์ ปรากฏการณ์เชิงแสงในโพรงสี่เหลี่ยมแบบเนสต์ระดับไมโครเมตร
 นักศึกษา นายรังสรรค์ จอมทะรักษ์
 รหัสประจำตัว 52650155
 ปริญญา ปรัชญาดุษฎีบัณฑิต
 สาขาวิชา ฟิสิกส์ประยุกต์
 พ.ศ. 2558
 อาจารย์ที่ปรึกษา รองศาสตราจารย์ ดร. ปรีชา ยุพาพิน
 อาจารย์ปฏิบัติหน้าที่แทนที่ปรึกษาวิทยานิพนธ์หลัก ดร. วรการ นียากร

บทคัดย่อ

ในงานวิจัยนี้เป็นการศึกษาคุณลักษณะการส่งผ่านสัญญาณแสงผ่านโพรงสี่เหลี่ยมแบบเนสต์ระดับไมโครเมตรที่เชื่อมต่อกับเกรตติง โดยระบบที่ออกแบบนี้ประกอบด้วยเกรตติงที่มีความบกพร่องสองชั้นเชื่อมต่อกับโพรงสี่เหลี่ยมแบบเนสต์ระดับไมโครเมตร ในการจำลองผลโดยใช้แสงเกาส์เซียนมีค่าความยาวคลื่นกลาง 1.55 ไมโครเมตร จากการจำลองผลพบว่าสัญญาณเอาพุทพัลส์รีโซแนนซ์มีค่าหน่วงสัญญาณเวลาเมื่อพัลส์แสงเคลื่อนที่ผ่านโพรงสี่เหลี่ยมแบบเนสต์ระดับไมโครเมตร และเกรตติงที่มีลักษณะสมมาตรซึ่งทำให้เกิดสัญญาณรังสีคลื่นเซเรนคอฟชนิดไปข้างหน้าและย้อนกลับ

ต่อมาได้เพิ่มโพรงสี่เหลี่ยมแบบเนสต์ระดับไมโครเมตรเป็นสองวงเพื่อสร้างหัววัดสัญญาณความเร็วชนิดดอปเปอร์เลื่อนระดับไมโครเมตร ทำให้พัลส์แสงที่มีค่าความยาวคลื่นสองค่าเกิดขึ้นเมื่อพัลส์แสงเคลื่อนที่ผ่านเกรตติงที่มีความบกพร่องสองชั้น โดยที่โหมดการรั่วของสัญญาณแสงที่เกิดขึ้นในโพรงสี่เหลี่ยมแบบเนสต์ระดับไมโครเมตรนั้นสามารถสร้างสัญญาณหัววัดความเร็วชนิดดอปเปอร์เลื่อนในโดเมนความถี่ได้

คำสำคัญ : โพรงสี่เหลี่ยมแบบเนสต์ระดับไมโครเมตร, หัววัดความเร็วชนิดดอปเปอร์เลื่อนในโดเมนความถี่

Thesis Title	OPTICAL PHENOMENA IN NESTED MICRORING RESONATOR
Student	RANGSAN JOMTARAK
Student ID	52650155
Degree	Doctor of Philosophy
Program	Applied Physics
Year	2015
Thesis Advisor	Assoc. Prof. Dr. Preecha Yupapin
Thesis Acting Co-advisor	Dr. Worakarn Neeyakorn

ABSTRACT

This thesis presents the transmission behaviors of light pulse through the nested microrings and gratings. The system design is consisted of a two-defect grating incorporating nested microrings with connecting on to the uniform grating. In modeling, the Gaussian light pulse with central wavelength of $1.55 \mu\text{m}$ is input into the waveguide of nested microrings via the two-defect grating and the uniform grating. The resonant outputs from the two-defect grating are propagated through the nested microrings and uniform grating, where the time delay of pulses with different wavelengths through the system is obtained and distinguished by the uniform grating. From the resonant output obtained, it is found that the red-shifted and blue-shifted Čerenkov radiation is observed.

Finally, the micro Doppler shift velocimeter using two nested-microring resonators incorporating with two gratings is designed and simulated. Two wavelength light pulse can be generated by a single input wavelength source after travelling through the two defect grating. Whispering gallery mode of light pulses is localized within the nested-microring resonators, which can be used to form the two point probe Doppler shift velocimeter. The shifted frequency (velocity) can be obtained by the difference of optical path length between two point probes, where the relative velocity of Doppler frequency shift velocimeter can be obtained. Output the light absorption behaviors can also be investigated by the different light spectrum.

Keywords: Nested microring resonator, Čerenkov effects, Doppler shift velocimeter.

ACKNOWLEDGEMENTS

While I have worked on this thesis for over three years, several people have contributed to this effort directly and indirectly. I would like to express my thankfulness to all of them.

No student thesis is achievable without the guidance and assistance of the thesis advisor. It was fortunate to have Assoc. Prof. Dr. Preecha P. Yupapin as my thesis advisor. His patient guidance, encouragement and enthusiasm throughout the development of my thesis were highly prized.

My profound gratitude must go to my parents, my wife, and my son for infinite encouraging and understanding me. They have always been there for me through this thesis. With their love, Nothing can stop me from working on this thesis. Special thanks are due to my best friends for their support. Some of them shared my insanity of doing a doctoral degree.

I would like to acknowledge Suan Dusit Rajabhat University, Bangkok, Thailand for granting the Thailand Ph.D. Program at Faculty of Science, King Mongkut's Institute of Technology Ladkrabang, Bangkok, Thailand.

TABLE OF CONTENTS

	Pages
Abstract in Thai	i
Abstract in English	ii
Acknowledgements	iii
Table of Contents.....	iv
List of Figures.....	vi
Chapter 1 Introduction.....	1
1.1 Transmission Characteristics of Optical Pulse	1
1.2 Čerenkov Radiation	3
1.3 Doppler Frequency Shift	4
1.4 Objectives of the Study	6
1.5 Scope of the Study	6
Chapter 2 Theory and Literature Reviews	7
2.1 Uniform Multilayer Grating	7
2.2 Microring Resonator	10
2.3 Doppler Frequency Shift	13
Chapter 3 Research methodology	23
3.1 Mathematical Model	23
3.2 Optiwave@FDTD Testing	25
Chapter 4 Results and Discussion	30
4.1 Transmission Characteristics of Optical Pulse in Nested Nonlinear Microring Resonators and Gratings.....	30

4.1.1 Two-defect Grating.....	31
4.1.2 Nested Nonlinear Microring Resonator (NMR).....	31
4.1.3 Transmission Behaviors of Light.....	33
4.1.4 Red-shifted and Blue-shifted Čerenkov Radiation.....	36
4.2 Doppler Shift Velocimetry Using Two Point Probe Nested-microring Resonators	38
4.2.1. Two Nested-Microring Resonator without Gratings.....	41
4.2.2 Two Nested-Microring Resonator with Gratings.....	44
4.2.3. Vary the Gap Coupling of Second-Nested Microring Resonator..	46
4.2.4 Vary Width of Waveguide and Nested Microring Resonators with gratings.....	52
Chapter 5 Conclusions and Suggestions	61
5.1 Transmission Characteristics of Optical Pulse in Nested Nonlinear Microring Resonators and Gratings.....	61
5.2 Doppler Frequency Shift Velocimeter	62
5.3 Future Work	62
References.....	63
Author Biography	70

List of Figures

Figure	Page
2.1 Model of uniform multilayer grating.....	7
2.2 OptiFDTD simulation results of two-defect grating coupled to uniform grating, (a) model, (b) Gaussian pulse propagation through the design model, and (c-f) the transmission and reflection intensity.....	10
2.3 The two basic configurations of microring resonators and their transmission spectra: (a) singly coupled microring, (b) doubly coupled microring, (c) spectrum at the <i>transmission</i> port, (d) spectrum at the <i>drop</i> port, source.....	12
2.4 A general result from FDTD simulation of the pulse propagating in the waveguide and coupling to the microring.....	13
2.5 (a) Schematic diagram of transmission behaviors of light in microring coupled to multilayer gratings, where $\Lambda = 0.2\mu\text{m}$ ($H = 0.1\mu\text{m}$ for InP material, $L =$ $0.1\mu\text{m}$ for InGaAsP material), $d_D = 0.2\mu\text{m}$ ($D = \text{GaAs}$ material) (b) output simulation results (c) 1D-profile and (d) 3D-profile of the light propagation in the model design by using OptiFDTD@optiwave commercial	15
2.6 (a) Schematic diagram of transmission behaviors of light in nest-microring coupled to multilayer gratings, where $\Lambda = 0.2\mu\text{m}$ ($H = 0.1\mu\text{m}$ for InP material, $L = 0.1\mu\text{m}$ for InGaAsP material), $d_D = 0.2\mu\text{m}$ ($D = \text{GaAs}$ material) (b) output simulation results (c) 1D-profile and (d) 3D-profile of the light propagation in the model design by using OptiFDTD@optiwave commercial software.....	16

- 2.7 (a) Schematic diagram of transmission behaviors of light in microring coupled to multilayer gratings without multilayer at the end of waveguide, where $\Lambda = 0.2\mu\text{m}$ ($H = 0.1\mu\text{m}$ for InP material, $L = 0.1\mu\text{m}$ for InGaAsP material), $d_D = 0.2\mu\text{m}$ ($D = \text{GaAs}$ material) (b) output simulation results by using OptiFDTD@optiwave commercial software..... 17
- 2.8 (a) Schematic diagram of transmission behaviors of light in single nested microring coupled to multilayer gratings, where $\Lambda = 0.2\mu\text{m}$ ($H = 0.1\mu\text{m}$ for InP material, $L = 0.1\mu\text{m}$ for InGaAsP material), $d_D = 0.2\mu\text{m}$ ($D = \text{GaAs}$ material) (b) output simulation results (c) 1D-profile and (d) 3D-profile of the light propagation in the model design by using OptiFDTD@optiwave commercial software..... 18
- 2.9 (a) Schematic diagram of transmission behaviors of light in two microring coupled to waveguide, where waveguide width, $w = 0.1\mu\text{m}$, radii of microring, $R = 2.7\mu\text{m}$ (b) output simulation results (c) 1D-profile and (d) 3D-profile of the light propagation in the model design by using OptiFDTD@optiwave commercial software..... 19

2.10(a) Schematic diagram of transmission behaviors of light in two nested microring coupled to waveguide, where $\Lambda = 0.2\mu\text{m}$ ($H = 0.1\mu\text{m}$ for InP material, $L = 0.1\mu\text{m}$ for InGaAsP material), $d_D = 0.2\mu\text{m}$ ($D = \text{GaAs}$ material)	
(b) output simulation results (c) 1D-profile and (d) 3D-profile of the light propagation in the model design by using OptiFDTD@optiwave commercial software.....	20
2.11(a) Schematic diagram of transmission behaviors of light in two nested microring coupled to multilayer grating, where $\Lambda = 0.2\mu\text{m}$ ($H = 0.1\mu\text{m}$ for InP material, $L = 0.1\mu\text{m}$ for InGaAsP material), $d_D = 0.2\mu\text{m}$ ($D = \text{GaAs}$ material)	
(b) output simulation results (c) 1D-profile and (d) 3D-profile of the light propagation in the model design by using OptiFDTD@optiwave commercial software.....	21
3.1 (a) Schematic of the nested microring resonator in InGaAsP/InP for higher and lower layers, respectively and (b) diagram of transmission and reflection light pulse.....	23
3.2 Scheme of microring resonator. g : gap coupling, w_i : waveguide width, R : microring resonator radius $4.7\mu\text{m}$	26
3.3 The model of microring for OptiFDTD test.....	27
3.4 The simulation results of microring for OptiFDTD commercial software test....	27

Trichosporon

Trigonopsis

4.3 การคัดเลือกยีสต์ที่มีการสะสมไขมันในเซลล์ปริ
การคัดเลือกยีสต์ที่มีการสะสมไขมันในเซลล์
20 ของซีวามวล (Ratlledge, 1979) โดยมียีสต์ *S. cere*
ในเซลล์เป็นตัวควบคุม โดย *S. cerevisiae* มีการสะสม
(Martinez และคณะ, 2016) เมื่อวัดค่าการเรืองแสง
และคณะ (2012) พบว่ามียีสต์ 74 ไอโซเลตที่มีค่า
4.27) ดังนั้นจึงจัดว่าเป็นยีสต์ที่ไม่มีการสะสมไขมันใน

ชน

วันที่

	ดำเนินการเพิ่ม	Yes	No	
20	ใส่บทคัดย่อใน Tag 520			
21	รวมไฟล์ตามลำดับ 1-19			วันที่
22	พิมพ์บทคัดย่อใน MS Word			วันที่

3.5	Simulation results of resonances peak in 3D view (first column) and 2D view (second column) by using OptiFDTD where (a) $w_1 = w_2 = 500\text{nm}$, $g = 0$, (b) $w_1 = w_2 = 500\text{nm}$, $g = 40\text{nm}$, (c) $w_1 = w_2 = 500\text{nm}$, $g = 120\text{nm}$, (d) $w_1 = w_2 = 500\text{nm}$, $g = 300\text{nm}$, and (e) $w_1 = 350\text{nm}$, $w_2 = 500\text{nm}$, $g = 40\text{nm}$.	28
3.6	Output resonances of single microring resonator for very gap coupling.....	29
4.1	Schematic diagram of transmission behaviors of light in nested nonlinear microring resonator and gratings.....	30
4.2	Shows the transmittance of two-defect multilayer and uniform grating, where two optical tweezers are occurring in two-defect multilayer and seen.	32
4.3	Shows the transfer function of transmission behavior light of nested nonlinear microring resonator.....	33
4.4	The transmission behaviors of light pulses in the nested nonlinear microring Resonators.....	34
4.5	The output power of the output port of the transmission light pulse in frequency domain range.....	35
4.6	The output intensity is detected in frequency domain at the point out1, out2, and out3 in Figure. 4.1 (Inset) the output intensity of nested nonlinear microring resonator and gratings, which is range from 169THz – 181THz.....	36
4.7	Shows the relationship between normalized intensity output and input, where (a) out1, (b) out2, and (c) out3.....	37

4.8 Shows the FFT results of two-defect modes, where (a) the first and (b) the second defect modes for two-defect grating.....	38
4.9 Schematic diagram of the nested microring resonator.....	40
4.10 Shows the WGMs of light pulses at the center, where (C ₁) and second (C ₂) are the first and second nested-microring resonators without gratings, respectively.....	42
4.11 The transmission (out) and circulation (circulate) of light intensity when propagate through.....	43
4.12 The WGMs of light pulse detect at the center of first (C ₁) and second (C ₂) nested microring resonator with gratings.....	44
4.13 The transmission (out) and circulation (circulate) of light intensity when propagate through (a) the first and (b) second nested microring resonators with gratings.....	45
4.14 The circulate intensity of the second nested-microring resonator with gratings for varies gap coupling. (inset) The profile of light intensity was traveling through the system design.....	47
4.15 The transmit (output) intensities are detect at the second nested-microring resonator with gratings for varying gap coupling from 0 – 400nm.....	48
4.16 The transmit (output) intensities are detect at the first, and second nested-microring resonator with gratings for varying gap coupling of the second nested-microring resonator.....	50

4.17 The circulate intensity passes through the second nested-microring resonator with gratings for varies gap coupling.....	51
4.18 The discrete flourier transform (DFT) of electric fields in y -direction for four optical waveguides design for vary the bus waveguide and nested MRR widths	52
4.19 The profile of light propagation in optical waveguides.....	53
4.20 The transmit (output) intensity for the bus waveguide width $w_2 = 1.0\mu\text{m}$ and the nested-microring width $w_1 = 0.5\mu\text{m}$	54
4.21 The transmit (output) intensity for the bus waveguide width $w_2 = 1.0\mu\text{m}$ and the nested-microring width $w_1 = 0.3\mu\text{m}$	55
4.22 The transmit (output) intensity for the bus waveguide width $w_2 = 0.5\mu\text{m}$ and the nested-microring width $w_1 = 0.3\mu\text{m}$	56
4.23 The transmission (output) and circulation intensities for varying the width of nested-microring (w_1) and bus waveguide (w_2) in frequency range 170 – 172THz.....	57
4.24 The WGMs detect for vary the width of nested microring and bus waveguide for (a) first and (b) second of nested-microring resonators with gratings.....	59

Chapter 1

Introduction

The optical phenomena in nested microring resonator are transmission characteristic of optical pulse, Čerenkov radiation, and Doppler frequency shift by cw Gaussian input light pulse. There is phenomena investigated in this thesis.

1.1 Transmission Characteristics of Optical Pulse

Optical trapping has become the promising technique of particle trapping and transportation, where the use of such a technique for nanoparticle trapping has been confirmed in both theory and experimental investigations [1–6], which can be used in many applications. For examples, the most interesting works have reported about the trapping of single 1 μm -sized polystyrene particles using the evanescent field of waveguide junctions connecting a sub-micrometer-sized input-waveguide and a micrometer-sized output-waveguide [2, 3]. The trapping tool generated by a modified add-drop filter known as a PANDA ring resonator has also been reported by Yupapin and his colleagues [4], where they have proposed a novel drug delivery system (DDS) by using a PANDA ring to form, transmit and receive the microscopic volume by controlling some suitable ring parameters, while the optical vortices (gradient optical field/well) can be generated and used to form the trapping tool in the same way as the optical tweezers. There is another technique that can also be used to form the particle trapping tools (optical tweezers) by using optical grating and shown many interesting results [7–11], where one of them has reported convincing technique of the anti-resonant reflecting, narrow-band, protein sensing. The grating guiding properties have also been investigated, in which the guiding conditions were studied for the Bragg and the ARROW-type fibers [7], showed equivalence in guiding principle between the in-phase condition at the core-cladding boundary and the anti-resonant reflection condition at each round trip in the 1D and cylindrically symmetric 2D structures with periodic cladding, which is

shown that the in phase condition is equivalent to a generalized quantum well structure (QWS) condition. The another work has been reported the study of reflection and group delay characteristics of the coupled ring reflector (CRR) [9]. It is consisted of two identical microrings coupled to each other and to a bus waveguide providing feedback, which is analytically and numerically investigated under loss-free and lossy conditions, that is subject to arbitrary (asymmetric) positioning of the couplers. This is allowed for a variable coupling strength, the spectral locations, where the extreme values of the reflectivity occur as well as its bandwidth are determined and their sensitivity to be loss evaluated, where the critical coupling conditions are determined by the shape and the turning points of the reflectance spectrum and their sensitivity to loss. Recently, Lu *et al* [12] have used a double microring resonator reflector for transmission and group delay is investigated. A microring resonator with an integrated Bragg grating [13, 14] can be enhanced the coupling efficiency between silicon-microring resonator, single-mode fiber and the gap coupling. The transmission properties of two nonlinear defects were investigated based on the nonlinear transfer matrix method [15–18]. Lamprecht *et al* [16] have used the metal nanoparticle grating for the influence of dipolar particle interaction on the plasmon resonance.

In this thesis, the Gaussian light pulse is used as the input optical pulse, where the transmission behaviors of light in multilayer nonlinear microring resonators and gratings have been investigated. The results have shown that the transmitted light pulses can be used to trap and inject particles into the multilayer nonlinear microring resonator, where the output particles can be retrieved by using the output uniform grating. One of the interesting aspects of the outputs is the transmission light pulse characteristics of the input and output ends, where it has a wide range of stop-band, which means that there is no particle transmission. The Čerenkov radiation of the two transmitted points is also seen, which can be used to study the wavelength-shifted, phase-matched, red-shifted and blue-shifted light [19–22], where Du *et al* [20–21] have also theoretically studied of Čerenkov second harmonic generation based-on lithium niobate that higher conversion efficiency, in which the Čerenkov radiation has been generated at 850 nm in higher-order-mode fiber with low pulse energy 3nJ and energy conversion efficiency up to 60% [22]. In this investigation, I found that the red-shifted and blue-shifted Čerenkov radiation can

be distinguished and seen, which can be useful for various applications such as Čerenkov sensing and, imaging fast and slow light applications.

1.2 Čerenkov Radiation

Čerenkov radiation is one of the signals produced by interactions between charged particles and medium [19, 23]. In general, the Čerenkov radiation has been appearance when the charged particle traveling through the dielectric medium at a speed faster than the phase velocity of light in that medium. Čerenkov radiation has since been studied in theoretical and experimental in one-dimensionally periodic multilayer stacks [24], photonic crystals [19, 25], fiber optics [23, 26–27], channel waveguide [21, 22], coaxial slow-wave structure [28], photonic crystal fiber [29], bulk birefringent quadratic medium [30], metamaterials [31]. Reflection of the produced radiation from the layer interfaces has been taken into account and absorption of radiation for Čerenkov radiation due to the passage of fast electrons through layered in one-dimensionally periodic multilayer stacks [24]. In photonic crystal, the speed of light pulse is $v = 0.6c > v_c$ the Čerenkov radiation has been sharp forward-pointing cone [19] when c is light velocity in vacuum and v_c is phase velocity. Čerenkov radiation has been generated at 850 nm in higher-order-mode fiber with low pulse energy 3nJ and energy conversion efficiency up to 60% [26] from the input light source (66% photon conversion efficiency). Fiber-optics radiation sensors for detecting the Čerenkov intensity light pulse as functions of irradiated length, irradiation angle, and thickness of various scatterers has been studied by Lee et al [27].

In applications, fiber-optic Čerenkov radiation sensor [32-33] without an organic scintillator to measure Čerenkov radiation is induced by therapeutic as a function of the dose rate of the proton beams. In industrial electron linacs [34] has been used the Čerenkov detector for half-value layer (HVL) measurement with detection threshold in the low energy range. Based-on Čerenkov radiation has been used in the nuclear imaging for Čerenkov luminescence light signal from radionuclides [35]. The optical fibers have been the Čerenkov detector design [36] for imaging in radiation therapy. The Čerenkov radiation generated in the fiber-optics radiation sensors (FORS) by irradiation of pure thermal neutron beams were measured in different depths of polyethylene [37] for detecting thermal neutrons in high temperature conditions.

My previously research [38], shows the red-shifted and blue-shifted Čerenkov radiation by using the Gaussian light pulse traveling through the nested nonlinear microring resonators and gratings system. In this research, I found that the red-shifted and blue-shifted Čerenkov radiation can be distinguished and seen, which can be useful for various applications such as Čerenkov sensing and, imaging fast and slow light applications.

1.3 Doppler Frequency Shift

Doppler frequency shift velocimeter is a standard technique for velocity measurement of moving targets in various research fields and industries. Maru *et al* has proposed the laser Doppler velocimeter (LDV) by using Mach-Zehnder interferometers for wavelength-insensitive [39] and small wavelength sensitivity [40], two-dimensional directional discrimination by monitoring scattered beams in different directions [41], two-dimensional LDV using polarized beams and 90° phase shift for discrimination of velocity direction [42], non-mechanical scanning laser Doppler velocimetry with sensitivity to direction of transverse velocity component using optical serrodyne frequency shifting [43], two-point velocity measurement using diffraction grating elements for integrated multi-point differential [44, 45].

Li *et al* [46] has proposed the Doppler effect-based fiber-optic (FOD) sensor and its application in ultrasonic detection on the surface of aluminum-alloy plate to generate ultrasonic wave. The sensitivity was direction-independent and directly proportional to the effective sensing length of the fiber optic sensor. FOD sensor can be made in many shapes such as circular loop, U-shape, and elongated circular loop.

Rodrigo and Pedersen [47] has proposed the monostatic coaxial $1.5\mu\text{m}$ laser Doppler velocimeter using a single frequency laser ($\lambda = 1.5\mu\text{m}$) and a high-finesse scanning Fabry-Perot interferometer. The sensitivity can be increased to unwanted back reflections in coaxial arrangement several order of magnitude of a simple circulator design.

Walther and Koch [48] has proposed the transverse motion as a source of noise and reduced correlation of the Doppler phase shift in spectral domain OCT. The certain velocities and Doppler angles no correlation of the phases of sequential A-Scans exists, even though the signal does not vanish. The noise of the Doppler phase shift behaves for oblique movement, the standard deviation is determined as a

function of the correlation quotient and the number of complex Doppler data averaged.

Varghese *et al* [49, 50] has proposed the discrimination between Doppler-shifted and non-shifted light in coherence domain path length resolved measurements of multiply scattered light and measurement of particle flux in a static matrix with suppressed influence of optical properties by using low coherence interferometry. Optical path length distributions of Doppler shifted and un-shifted light, spanning a range from 0 to 6 mm are measured in a two layer static and dynamic turbid phantom, with a superficial static layer placed on top of a dynamic turbid medium having identical optical properties. The low coherence interferometry scheme in the fiber optic Mach-Zehnder configuration enables optical Doppler or dynamic light scattering measurements of dynamic media embedded in a static medium.

Bai *et al* [51] has proposed the heterodyne Doppler velocity measurement of moving targets by mode-locked pulse laser. The coherent beat frequency of the signal light reflected by target and local oscillation light occurred on the surface of the detector. The velocity measurement has a high precision and the error on average is within 0.4m/s.

Hirschberger and Ehret [52] have proposed the simulation and high-precision wavelength determination of noisy 2D Fabry-Perot interferometric rings for direct-detection Doppler lidar and laser spectroscopy.

Kervevan *et al* [53] has proposed the self-mixing laser Doppler velocimetry with a dual-polarization Yb:Er glass laser by using the radio-frequency spectrum with and without a Faraday rotator and a large beating note between the two modes to show the extension of the velocity range measurement.

In this section, I present the Doppler frequency shift velocimeter without discrimination by using two-deflected mode, unidirectional operation and reflection sensitivity two nested microring resonators. The relative velocity was measurement the reflection and transmission in two nested-microring resonators for comparing. The simulation results are shown the Doppler frequency shift velocimeter of two nested-microring resonators with and without gratings. Moreover, I present the Doppler frequency shift velocimeter of the varied gap coupling of the second nested-microring resonators and varied the width of nested-microring resonators and bus waveguide.

1.4 Objectives of the Study

The objectives of the research are following

- 1) To study the transmission characteristics of Gaussian pulse in nested microring and grating.
- 2) To study the red-shifted and blue-shifted Čerenkov radiation by using the Gaussian pulse.
- 3) To study the small scale Doppler frequency shift velocimeter without discrimination by using two-deflected mode of grating.

1.5 Scope of the Study

The thesis is organized as follows. The theory and literature reviews are extensively studied in a uniform multilayer grating, microring resonator, and Doppler frequency shift (Chapter 2). An analytical a uniform multilayer grating model based on the electromagnetic wave is bounded in order to between layers in which the Goos-Hänchen shift will be occurred. Analytical results are compared with corresponding simulations and directly applied to solve the multilayer grating are coupled to the nested microring resonators for transmission behaviors of light.

Chapter 3 Shows the mathematical model of nested microring resonator. The OptiFDTD@Optiwave is tested for the transfer function of light pulse propagated through the microring resonator.

Chapter 4 is dedicated to simulation results. First, the transmission characteristics of optical pulse in nested nonlinear microring resonators and gratings are investigated for the light behavior. Next, the Doppler shift velocimetry using two point probe nested-microring resonators are shown. Furthermore, I present the design, and characterization of varies the gap coupling and the width of waveguide.

Chapter 5 concludes the thesis with an outlook on further work to be done in this field.

Chapter 2

Theory and Literature Reviews

2.1 Uniform Multilayer Grating

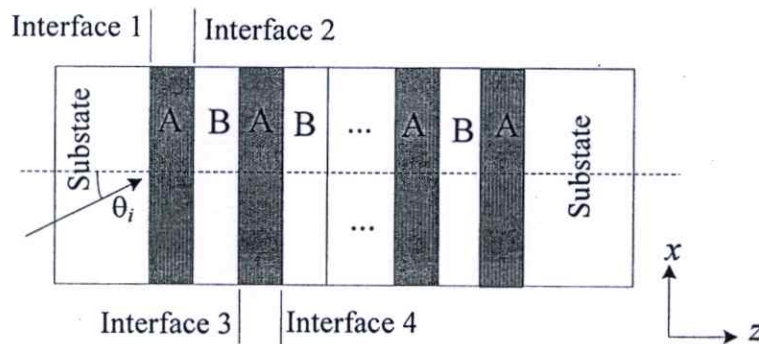


Figure 2.1 Model of uniform multilayer grating.

When incident light is incident on the interface of the optically denser medium and the optically thinner medium with the angle greater than the total reflection critical angle, the total reflection will be occurred. Due to the continuity conditions of the electromagnetic field, the boundary relationship of the electromagnetic field on the interface may not be broken off, thus the evanescent wave will penetrate into the optically thinner medium layer with a certain depth. The evanescent wave is an inhomogeneous wave, which can propagate along x -direction and vibrate along the z -direction. Taking x - z plane as the reference plane, the wave function can be expressed as

$$\begin{aligned}
 \vec{E}_i &= \vec{E}_i \exp[i(\vec{k} \cdot \vec{r} - \omega t)] \\
 &= \vec{E}_i \exp[i(k_x x + k_z z - \omega t)] \\
 &= \vec{E}_i \exp(-kz) \exp[i(k_x x - \omega t)]
 \end{aligned} \tag{2.1}$$

where \vec{E}_i and \vec{E}_t are the field intensity in the optically denser medium and the optically thinner medium respectively, \vec{k} is the incident light wave vector, $k_x = k \cdot n_D \cdot \frac{\sin \theta}{n_A}$ is the component in x -axis of the incident light wave vector, $k_z = \pm i k \sqrt{n_D^2 - \frac{\sin^2 \theta}{n_A^2}}$ is the component in z -axis of the incident light wave vector.

The amplitude of the evanescent wave will decay with the increment of the penetration depth, and when the amplitude decay to the 1/e of amplitude maximum value. The penetration depth z_d can be expressed as [25]

$$z_d = \left(k_D \sqrt{\sin^2 \theta - (n_A/n_D)^2} \right)^{-1} \quad (2.2)$$

Generally, the evanescent wave will penetrate into the optically thinner medium layer with a certain depth and then return to the incident medium. While if $d_A < z_d$, the evanescent wave will penetrate into the interface 2 and enter into the layer B, and due to the attenuation of evanescent wave, a single evanescent wave can-not propagate through the dielectric layer. The light in the layer B will penetrate the interface 3 with a certain distance, and then return to the dielectric layer B. The total reflection will occur constantly on the interfaces of the both sides for the layer B, in which the Goos-Hänchen shift will occur.

The dielectric layer B can be regarded as a F-P resonant cavity, thus the relationship between the resonant wavelength and the incident angle can be expressed as [25]

$$2 \cdot \frac{2\pi}{\lambda_d} n_B d_B \cos \theta_B + \frac{2\pi}{\lambda} \cdot (2\Delta) = 2k\pi \quad (k = 0, 1, 2, \dots) \quad (2.3)$$

Where the Goos-Hänchen shift Δ can be expressed as

$$\Delta = \frac{\lambda \tan \theta_B}{\pi (\sin^2 \theta_B - \sin^2 \theta_C)^{\frac{1}{2}}} \quad (2.4)$$

Where λ is the wavelength of the incident light. λ_d is the resonant wavelength. $\theta_C = \arcsin(n_A/n_B)$ is the total reflection critical angle at the interface 3.

Similarly, each periodical layer B in the PC all can be regarded as a resonant cavity. The electromagnetic wave among different defects are coupled, which results in the eigen-mode of defect mode splitting. Thus the PC $(AB)_m A$ may have m number of resonance cavities. Based on the tight-binding theory m defect modes can be obtained in the photonic band gap.

The electromagnetic waves at the interface on the continuity conditions of electromagnetic wave on the boundary, the electromagnetic field can be expressed as [25]

$$\begin{cases} E_i^+ + E_i^- = E_j^+ + E_j^- \\ H_i^+ \cos \theta_i - H_i^- \cos \theta_i = H_j^+ \cos \theta_j - H_j^- \cos \theta_j \end{cases} \quad (2.5)$$

where $H = \sqrt{\epsilon_0/\mu_0}nE$, then Eq.(2.5) can be given by

$$\begin{aligned} \begin{bmatrix} E_i^+ \\ E_i^- \end{bmatrix} &= \begin{bmatrix} 1 & 1 \\ n_i \cos \theta_i & -n_i \cos \theta_i \end{bmatrix}^{-1} \times \begin{bmatrix} 1 & 1 \\ n_j \cos \theta_j & -n_j \cos \theta_j \end{bmatrix} \cdot \begin{bmatrix} E_j^+ \\ E_j^- \end{bmatrix} \\ &= m_{ij} \begin{bmatrix} E_j^+ \\ E_j^- \end{bmatrix} \end{aligned} \quad (2.6)$$

where m_{ij} is the transmission matrix from dielectric i to j , which can be expressed as

$$m_{ij} = \frac{1}{2} \cdot \begin{bmatrix} 1 + \frac{n_j \cos \theta_j}{n_i \cos \theta_i} & 1 - \frac{n_j \cos \theta_j}{n_i \cos \theta_i} \\ 1 - \frac{n_j \cos \theta_j}{n_i \cos \theta_i} & 1 + \frac{n_j \cos \theta_j}{n_i \cos \theta_i} \end{bmatrix} \quad (2.7)$$

While in the single dielectric layer, the electric field can be connected with matrix

$$\begin{bmatrix} E_i^+ \\ E_i^- \end{bmatrix} = \begin{bmatrix} e^{-i\varphi} & 0 \\ 0 & e^{i\varphi} \end{bmatrix} \cdot \begin{bmatrix} E_i'^+ \\ E_i'^- \end{bmatrix} = m_i \begin{bmatrix} E_i'^+ \\ E_i'^- \end{bmatrix} \quad (2.8)$$

where m_i is the transmission matrix of dielectric layer i , $\varphi = k_i d_i \cos \theta_i$ is the phase difference, $k = 2\pi/\varphi$ is the wave number. [25]

The total characteristic matrix is composed of the boundary characteristic matrix and the internal characteristic matrix. Through the analysis above, for the multilayer structure mentioned above the total transfer matrix equation can be given by

$$\begin{bmatrix} E_i^+ \\ E_i^- \end{bmatrix} = M \begin{bmatrix} E_N^+ \\ 0 \end{bmatrix} = \begin{bmatrix} M_{11} & M_{12} \\ M_{21} & M_{22} \end{bmatrix} \cdot \begin{bmatrix} E_N^+ \\ 0 \end{bmatrix} \quad (2.9)$$

The transmission coefficient can be expressed as [25]

$$t = \frac{E_N^+}{E_i^+} = \frac{1}{M_{11}}. \quad (2.10)$$

In this thesis, I design the two defect mode of multilayer grating and multilayer coupled to straight waveguide at the end as shown in Figure 2.2. The schematic diagram of design is fixed $\Lambda = 0.2\mu\text{m}$ ($H = 0.1\mu\text{m}$ for InGaAsP material, $L = 0.1\mu\text{m}$ for InP material), $d_0 = 0.2\mu\text{m}$ ($D = \text{GaAs}$ material), respectively. The OptiFDTD simulation results of two-defect grating coupled to uniform grating as shown in Figure 2.2 I found that the resonance peak (filter peak) are generated around the center wavelength, $\lambda_0 = 1.35\mu\text{m}$, as see in Figure 2.2(c)-(f).

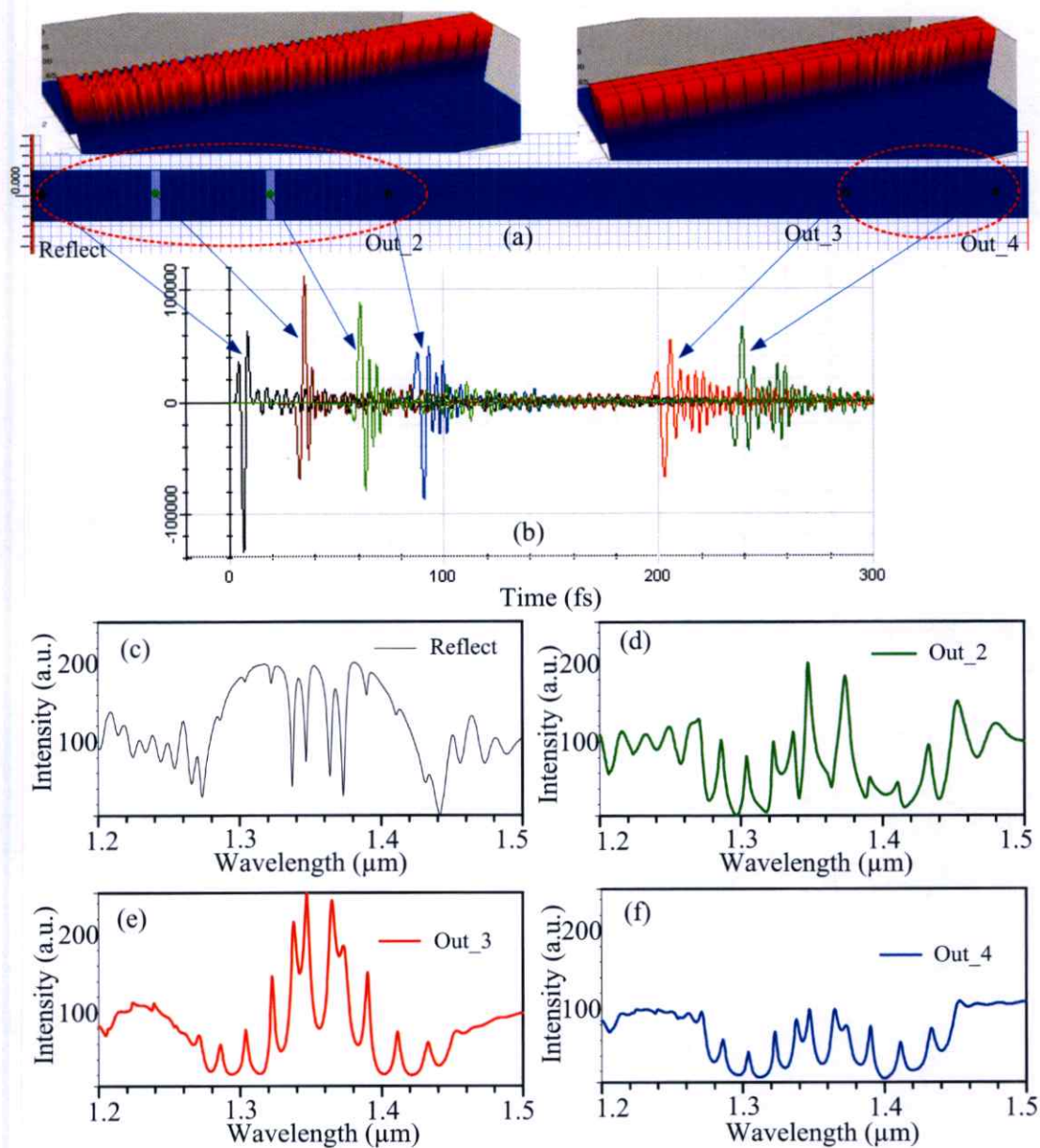


Figure 2.2 OptiFDTD simulation results of two-defect grating coupled to uniform grating, (a) model, (b) Gaussian pulse propagation through the design model, and (c-f) the transmission and reflection intensity.

2.2 Microring Resonator

A microring resonator essentially consists of a looped waveguide. Just like in a straight waveguide, the light is confined to the core and decays exponentially in the surrounding materials. When the phase shift after one round-trip in the microring is an integer multiple of 2π , the light will build up in intensity due to constructive

interference and will form a resonant mode of the resonator. The resonance condition becomes

$$\lambda_{res} = \frac{2\pi R n_{eff}}{m} = \frac{L n_{eff}}{m} \quad m \in \mathbf{Z} \quad (2.11)$$

where R is the outer radius of the microring and L is its circumference.

Microcavities are usually coupled to an input or excitation waveguide which excites the field in the resonator by the evanescent tail of the waveguide mode. Sometimes, the resonator is also coupled to an output or *drop* waveguide. The transmission spectrum of the input waveguide will show dips at the resonance frequencies of the microcavities, since at these frequencies energy is extracted from the waveguide to the ring. In the spectrum of the drop waveguide on the other hand, there will be peaks at these resonant frequencies. The configurations with and without drop port and the according spectra are shown in Figure 2.3.

The spectral distance between two modes with a subsequent mode number m is called the free spectral range (FSR) and is given by

$$FSR = \frac{\lambda^2}{2\pi R n_{eff}} \quad (2.12)$$

The width of the resonance peaks is described by their quality factor Q , defined as the ratio of the energy stored in the resonator to the energy loss per cycle. The Q factor can be calculated with by

$$Q = \frac{\lambda_{res}}{\delta\lambda_{FWHM}} \quad (2.13)$$

where $\delta\lambda_{FWHM}$ is the width of the peak (dip) at half of its maximum (minimum) value (FWHM = Full Width at Half Maximum/Minimum). A high Q factor thus corresponds to narrow spectral peaks.

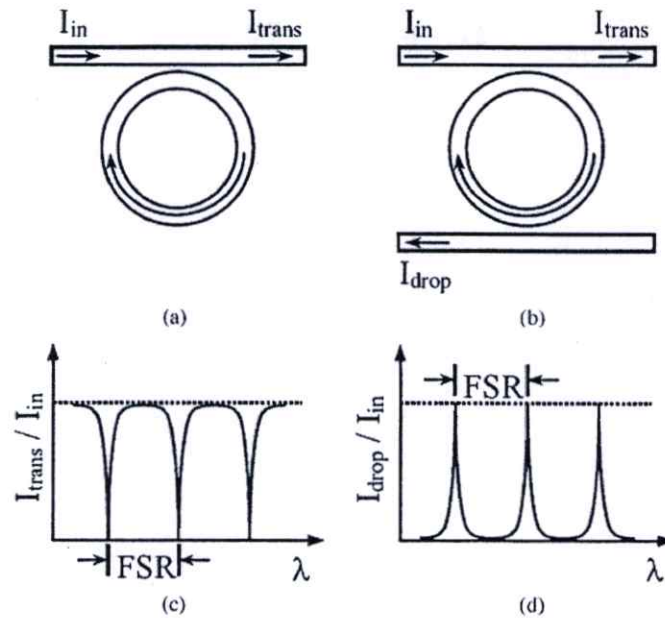


Figure 2.3 The two basic configurations of microring resonators and their transmission spectra: (a) singly coupled microring, (b) doubly coupled microring, (c) spectrum at the *transmission* port, (d) spectrum at the *drop* port, source: [74]

The width of the resonance peaks can also be described by the finesse F of the resonator, defined as

$$F = \frac{FSR}{\delta\lambda_{FWHM}} \quad (2.14)$$

From the resonance condition (2.11), it is derived that $\delta n_{eff}/n_{eff} = \delta\lambda_c/\lambda_c \approx 1/Q$ [74]. The detectable refractive index changes are thus inversely proportional to the quality factor of the cavity. Consequently, for a resonator to be used as a sensor, high Q factors are important to minimize the minimal detectable wavelength shift and therefore the sensor's sensitivity. To achieve high Q factors, all the resonator losses have to be minimized. Typical occurring losses in microring resonators are bending and surface losses. Surface losses are due to surface roughness and can be alleviated with better fabrication techniques. Bending losses will increase with smaller radii (since the mode is pushed outwards), while surface losses will be reduced due to the smaller round-trip lengths.

Nguyen and Norwood [54], have studied the label-free, single-object sensing with microring resonator by using OptiFDTD simulation, they considered the simulation of microring with $R = 20\mu\text{m}$, $d_R = d_W = 1\mu\text{m}$ and index $n_R = n_W = 1.46$ the simulation result as shown in Figure 2.4.

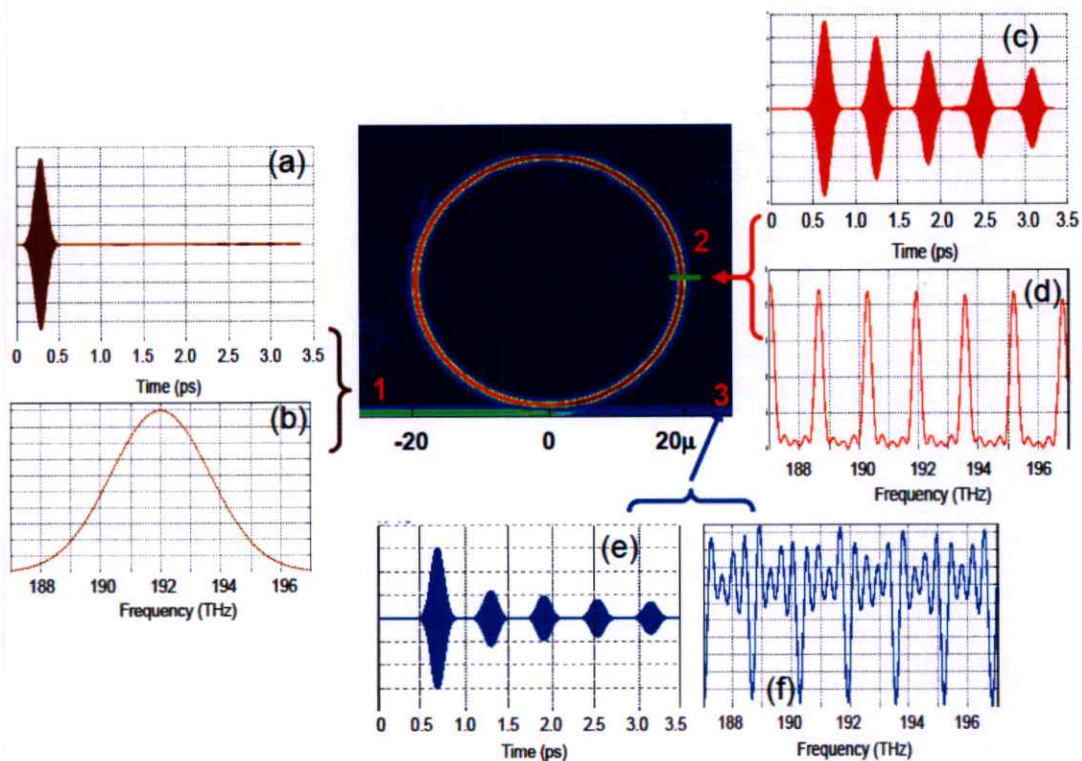


Figure 2.4 A general result from FDTD simulation of the pulse propagating in the waveguide and coupling to the microring. (a) E -field of the input pulse in time domain (TD), and (b) normalized intensity in frequency domain (FD). (c) E -field inside the cavity measured at position 2 in TD, and (d) relative intensity in FD showing the resonant modes of the ring without the sensing object. (e) E -field in TD and (f) transmission in FD (at position 3). Central: intensity of the light with frequency $f = 192$ THz which is closest to a resonant mode of the ring shown in (d). [54]

2.3 Doppler Frequency Shift

The Čerenkov effect is the existence of a certain kind of electromagnetic radiation when a particle is traveling through a medium at a superluminal velocity for that material. This can be understood through Huygens' Principle, when a wave source is traveling faster than the waves it emits. In this case, a linear shock wave forms results in a front of photons propagating through the material.

Doppler frequency shift velocimeter is a standard technique for velocity measurement of moving targets in various research fields and industries. Maru *et al* has proposed the laser Doppler velocimeter (LDV) by using Mach-Zehnder interferometers for wavelength-insensitive [39] and small wavelength sensitivity [40], two-dimensional directional discrimination by monitoring scattered beams in different directions [41], two-dimensional LDV using polarized beams and 90° phase shift for discrimination of velocity direction [42], non-mechanical scanning laser Doppler velocimetry with sensitivity to direction of transverse velocity component using optical serrodyne frequency shifting [43], two-point velocity measurement using diffraction grating elements for integrated multi-point differential [44, 45].

In the differential LDV, the beat frequency detected by the PD, F_D , is expressed as

$$F_D = \frac{2v_\perp \sin \psi}{\lambda} \quad (2.15)$$

where ψ is the incident angle of the beam to the object, v_\perp is the velocity of the object perpendicular to the bisector of the angles of the incident beams to the object, and λ is the wavelength. From this equation, if ψ appropriately changes depending on λ , the wavelength-insensitive operation can be expected. When F_D is to be insensitive to the wavelength around $\lambda = \lambda_0$, the derivative of F_D with respect to λ should be zero at $\lambda = \lambda_0$. From Eq. (2.15), this condition is expressed as

$$\left. \frac{d\psi}{d\lambda} \right|_{\lambda=\lambda_0} = \frac{\tan \psi_0}{\lambda_0} \quad (2.16)$$

where ψ_0 is the incident angle at $\lambda = \lambda_0$.

The Doppler frequency shift f_D induced by the target could be denoted as

$$f_D = \frac{2(v \cos \theta)}{\lambda} \quad (2.17)$$

where v is tangential velocity of the rotating plate, and θ is the angle between incident light and velocity. In the experiment, $\theta = 40^\circ$ [51]. Then Doppler frequency shift f_D calculated is 29.85 MHz. Using Eq. (2.17), the tangential velocity of the target is 20.73 m/s. Compared to actual speed, which is 20.58 m/s, the error is 0.15 m/s.

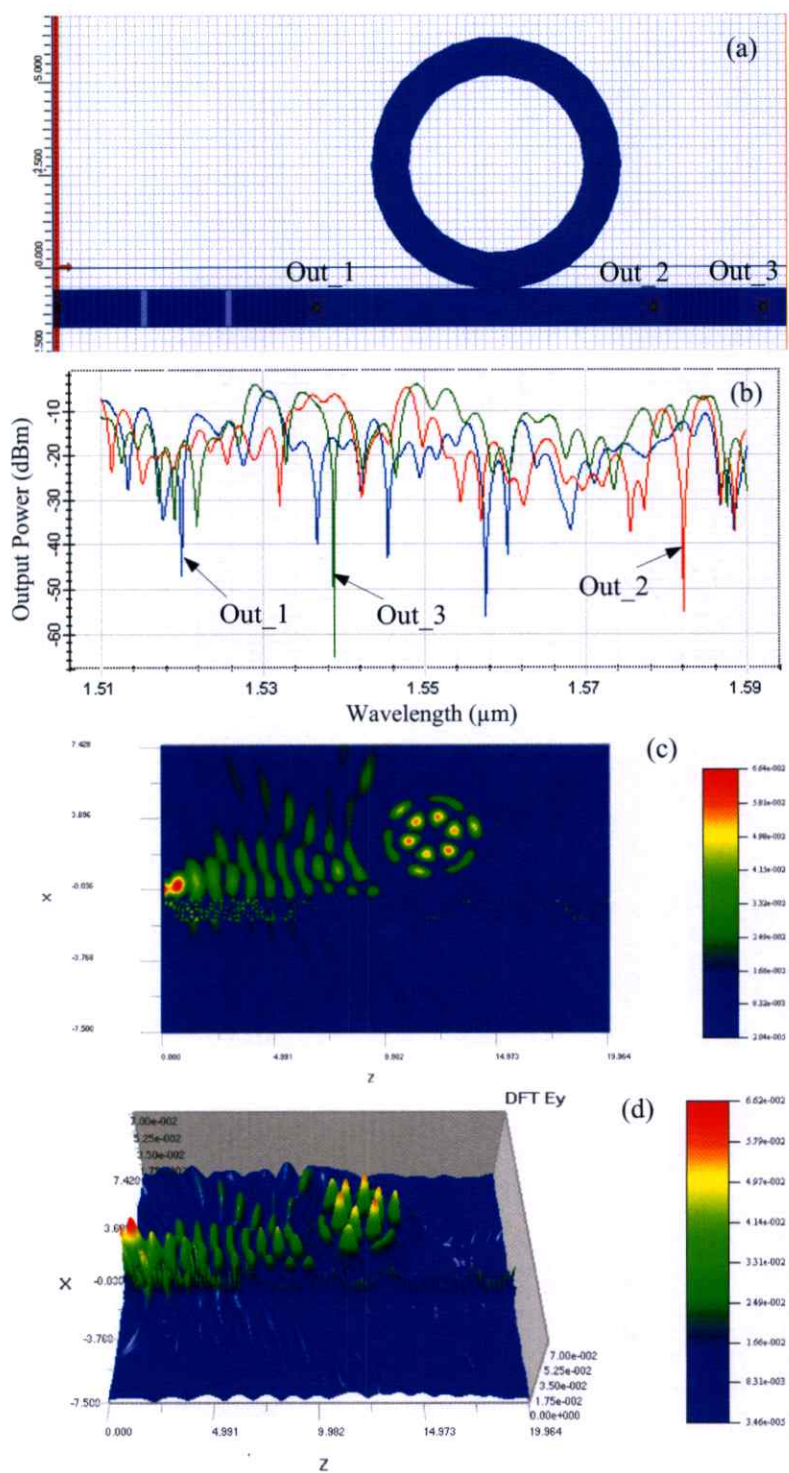


Figure 2.5 (a) Schematic diagram of transmission behaviors of light in microring coupled to multilayer gratings, where $\Lambda = 0.2\mu\text{m}$ ($H = 0.1\mu\text{m}$ for InGaAsP material, $L = 0.1\mu\text{m}$ for InP material), $d_D = 0.2\mu\text{m}$ ($D = \text{GaAs}$ material) (b) output simulation results (c) 1D-profile and (d) 3D-profile of the light propagation in the model design by using OptiFDTD@optiwave commercial software (KMITL License).

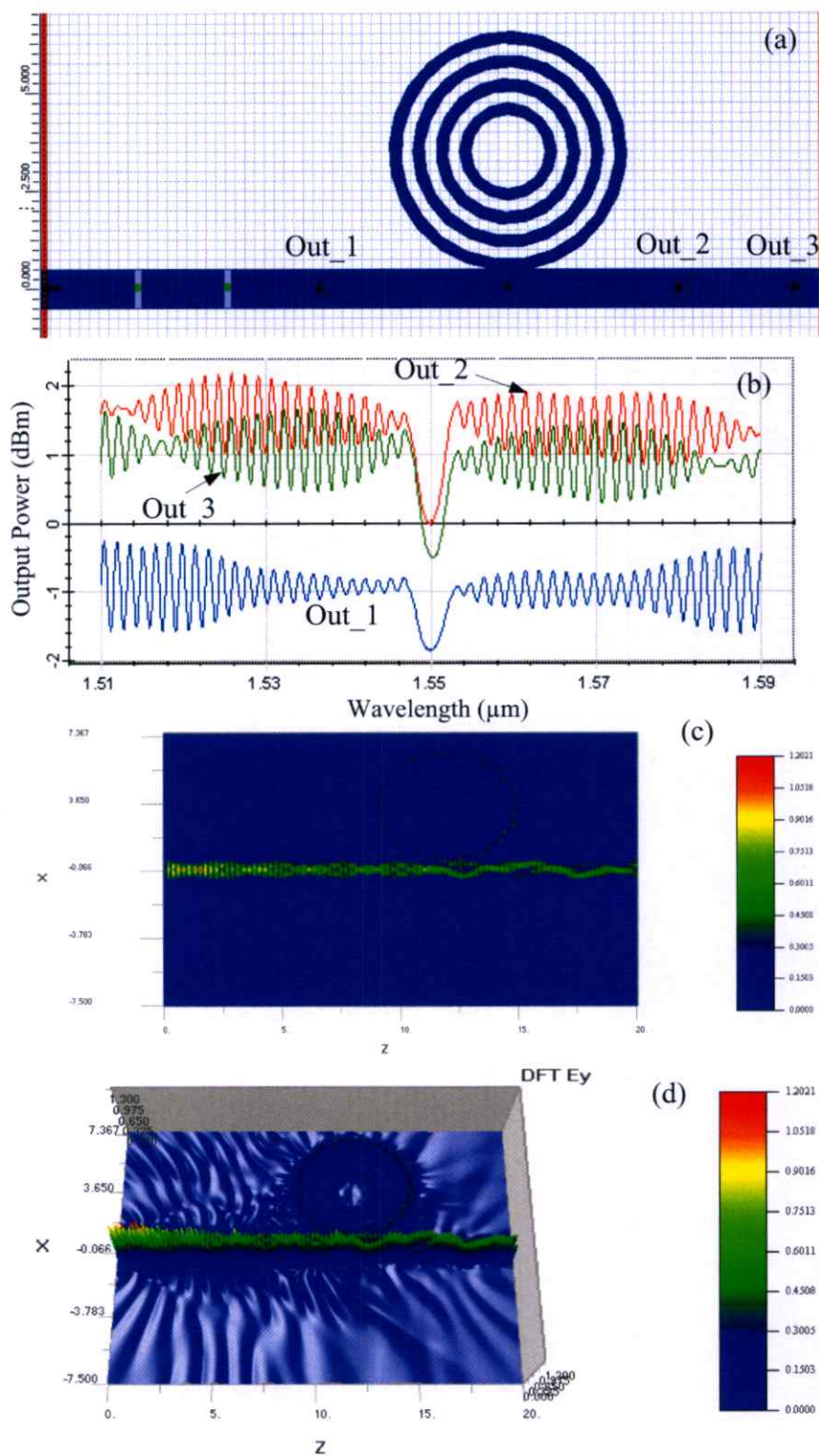
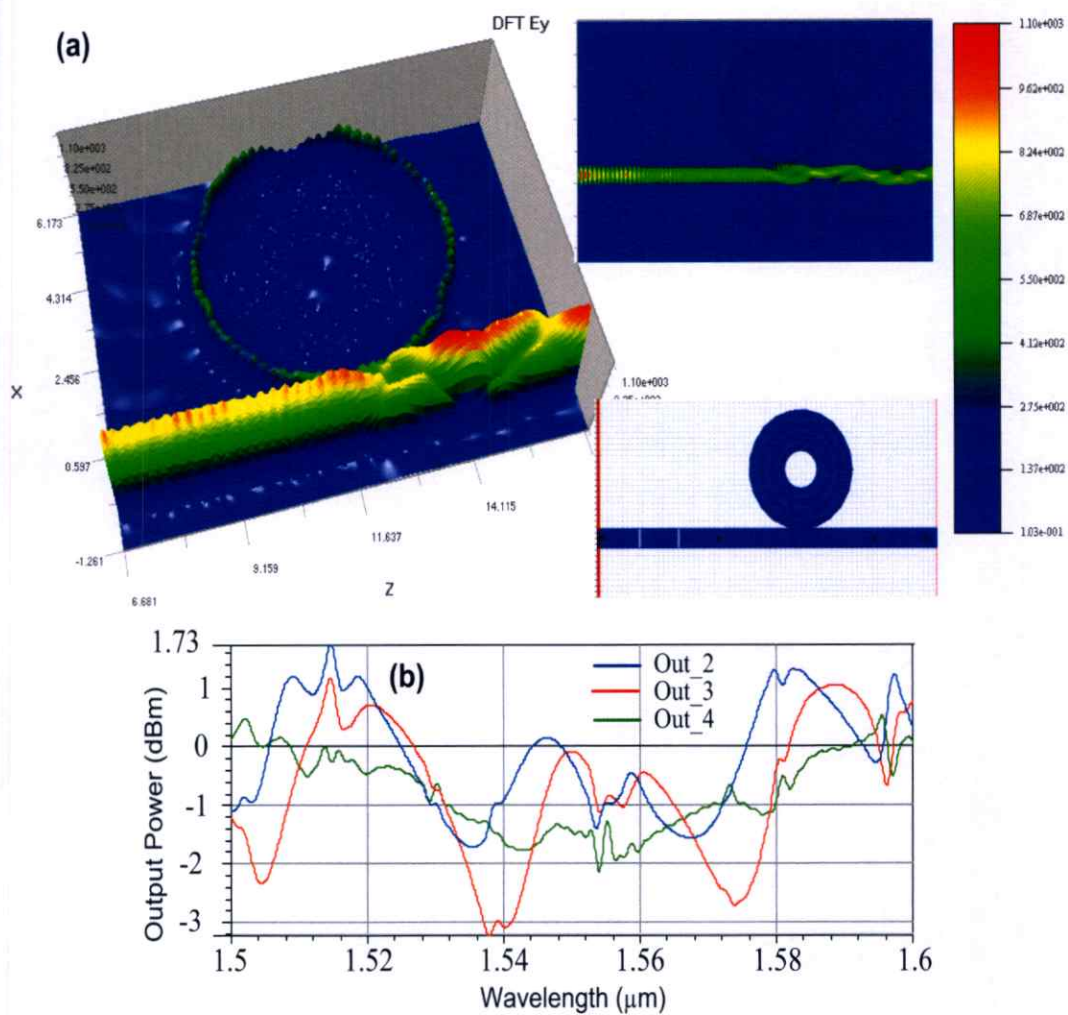


Figure 2.6 (a) Schematic diagram of transmission behaviors of light in nest-microring coupled to multilayer gratings, where $\Lambda = 0.2\mu\text{m}$ ($H = 0.1\mu\text{m}$ for InGaAsP material, $L = 0.1\mu\text{m}$ for InP material), $d_D = 0.2\mu\text{m}$ ($D = \text{GaAs}$ material) (b) output simulation results (c) 1D-profile and (d) 3D-profile of the light propagation in the model design by using OptiFDTD@optiwave commercial software (KMITL License).



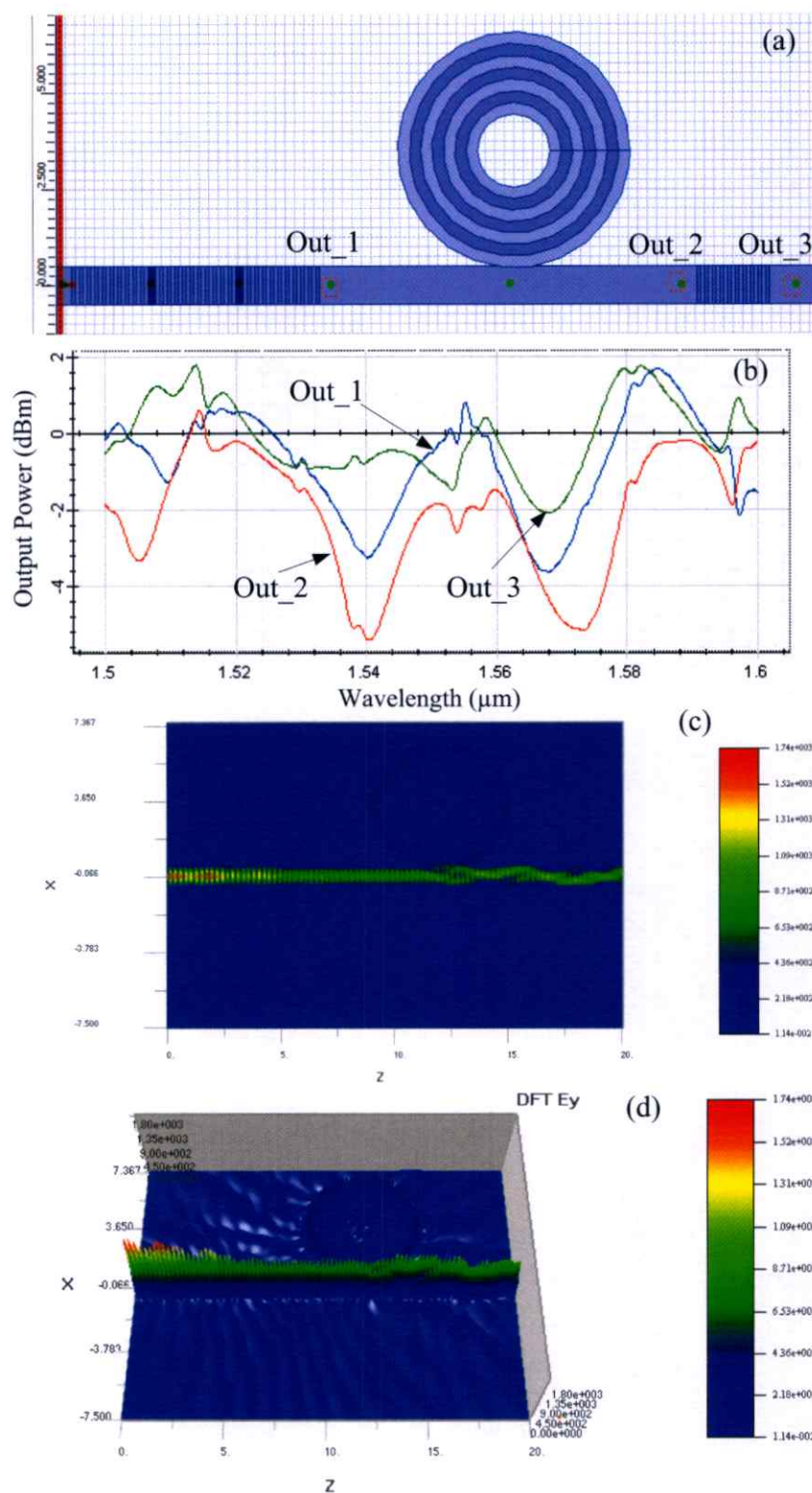


Figure 2.8 (a) Schematic diagram of transmission behaviors of light in single nested microring coupled to multilayer gratings, where $\Lambda = 0.2\mu\text{m}$ ($H = 0.1\mu\text{m}$ for InGaAsP material, $L = 0.1\mu\text{m}$ for InP material), $d_0 = 0.2\mu\text{m}$ ($D = \text{GaAs}$ material) (b) output simulation results (c) 1D-profile and (d) 3D-profile of the light propagation in the model design by using OptiFDTD@optiwave commercial software (KMITL License).

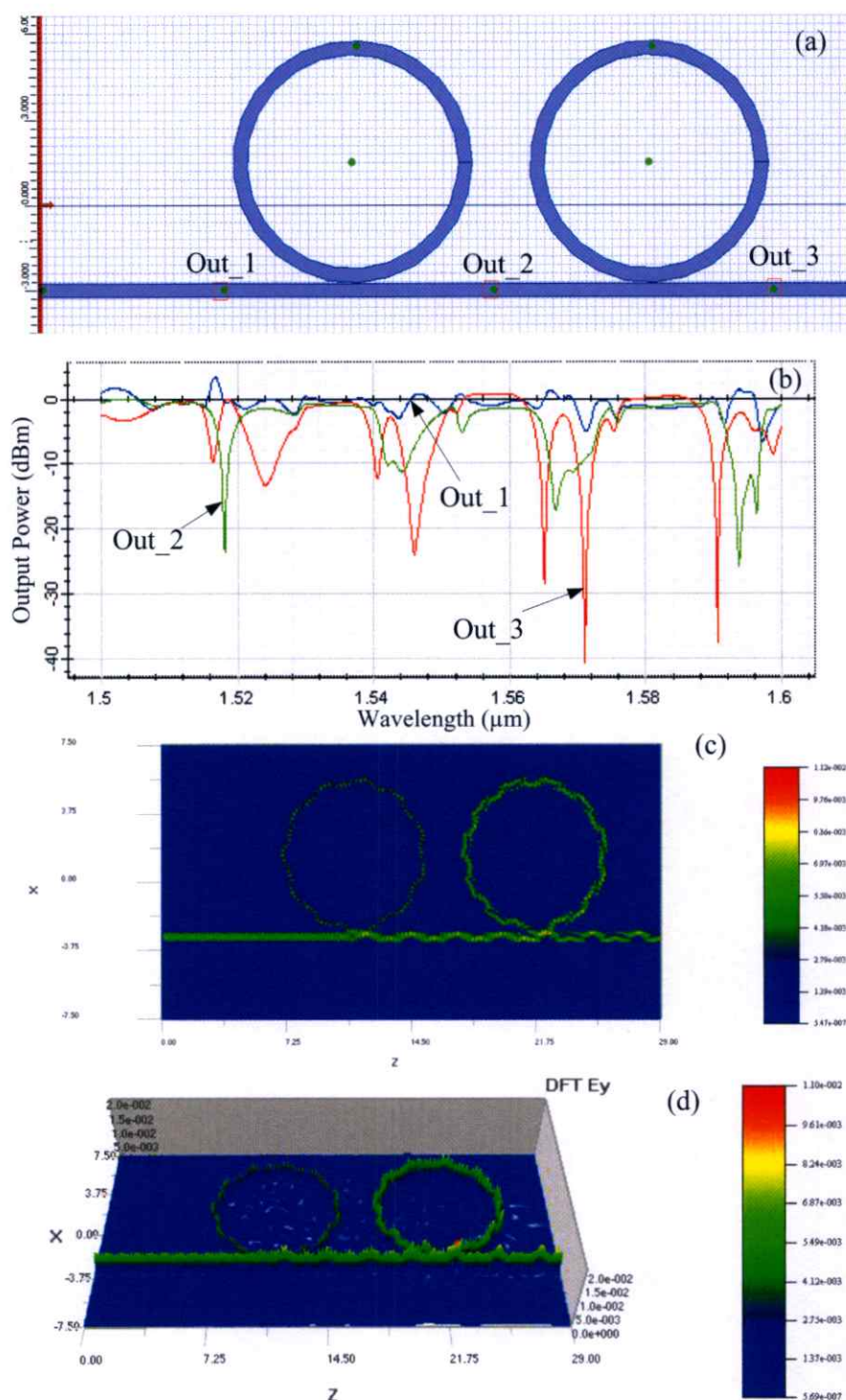


Figure 2.9 (a) Schematic diagram of transmission behaviors of light in two microring coupled to waveguide, where waveguide width, $w = 0.1\mu\text{m}$, radii of microring, $R = 2.7\mu\text{m}$ (b) output simulation results (c) 1D-profile and (d) 3D-profile of the light propagation in the model design by using OptiFDTD@optiwave commercial software (KMITL License).

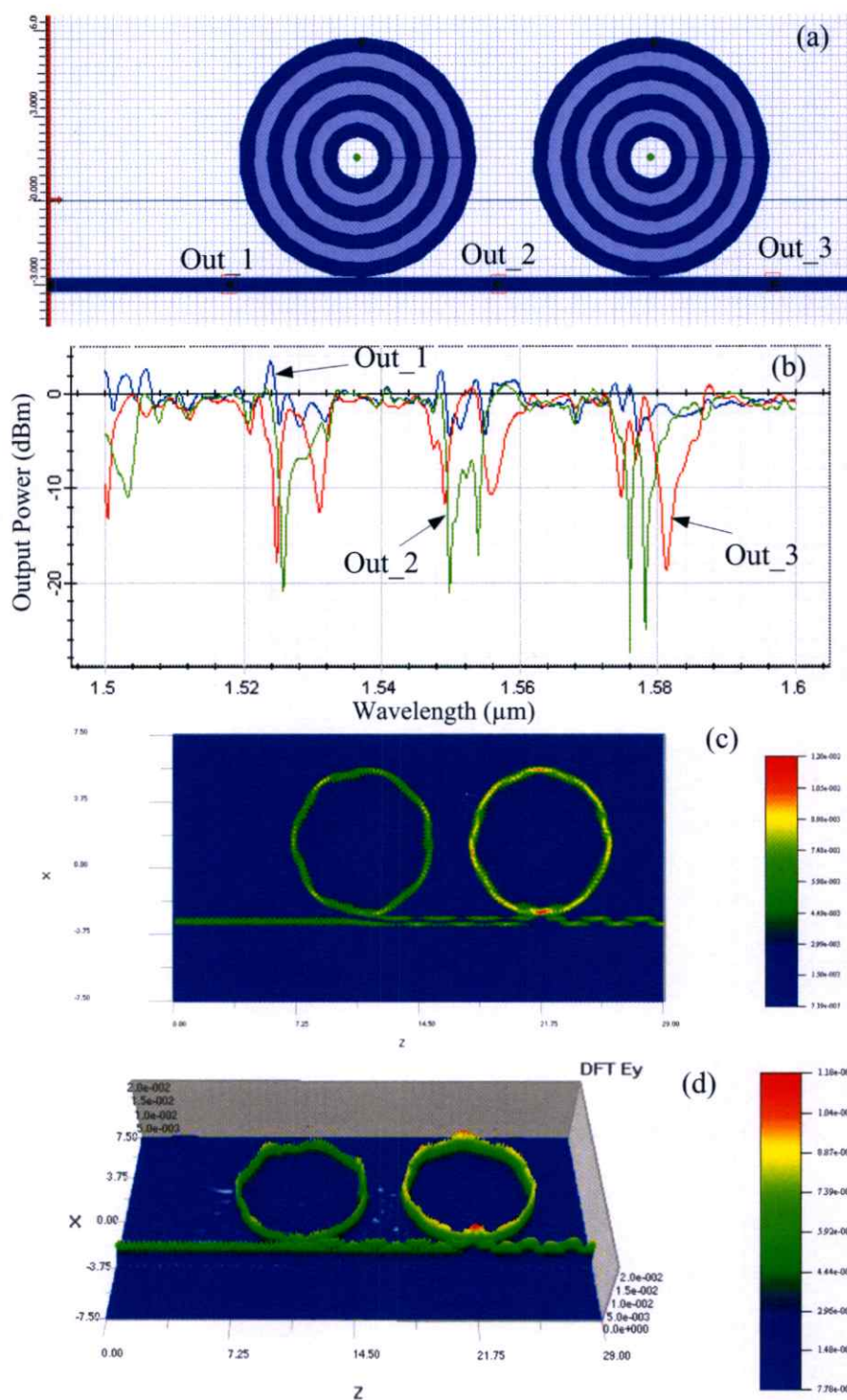


Figure 2.10 (a) Schematic diagram of transmission behaviors of light in two nested microring coupled to waveguide, where $\Lambda = 0.2\mu\text{m}$ ($H = 0.1\mu\text{m}$ for InGaAsP material, $L = 0.1\mu\text{m}$ for InP material), $d_D = 0.2\mu\text{m}$ ($D = \text{GaAs}$ material) (b) output simulation results (c) 1D-profile and (d) 3D-profile of the light propagation in the model design by using OptiFDTD@optiwave commercial software (KMITL License).

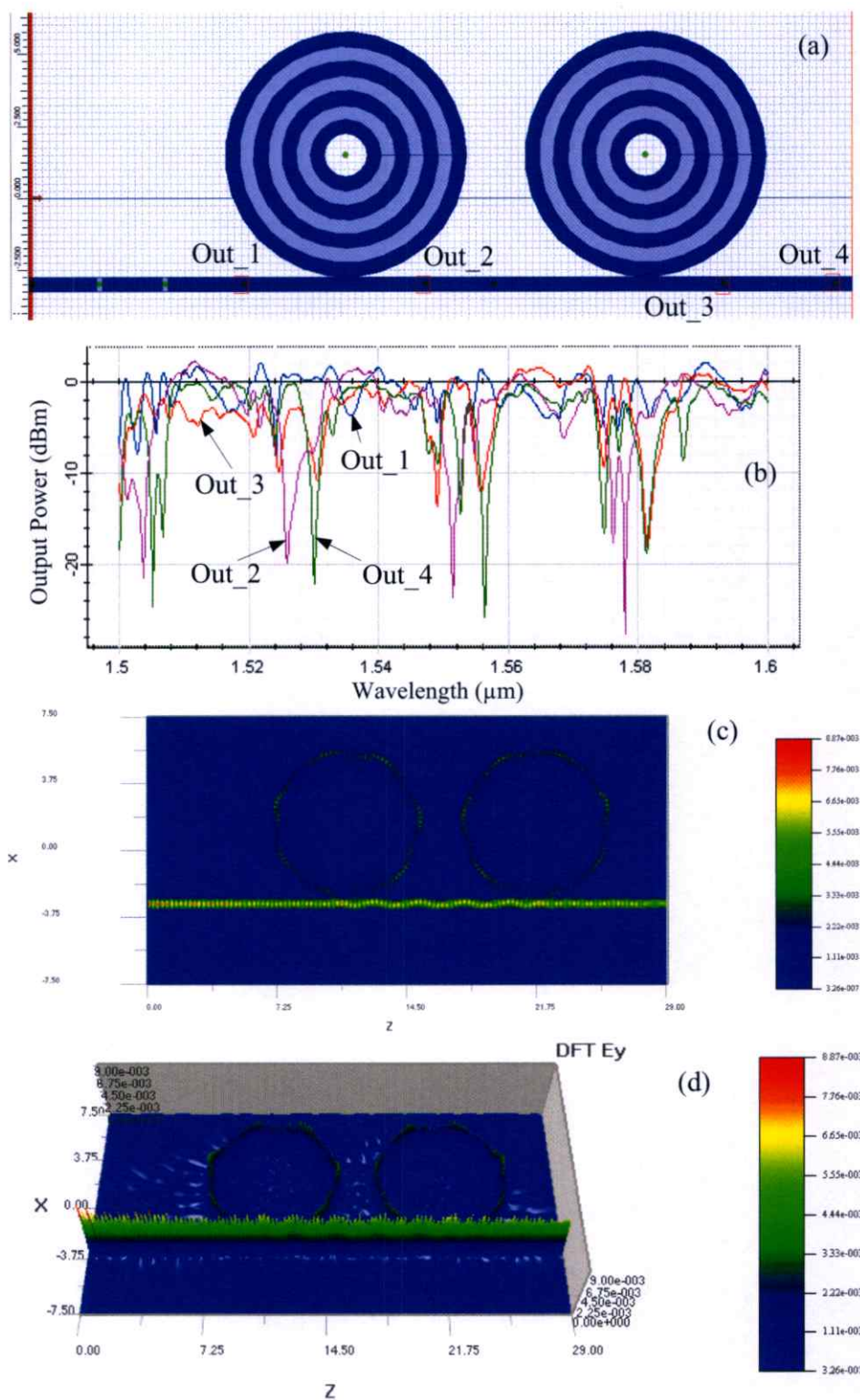


Figure 2.11 (a) Schematic diagram of transmission behaviors of light in two nested microring coupled to multilayer grating, where $\Lambda = 0.2\mu\text{m}$ ($H = 0.1\mu\text{m}$ for InGaAsP material, $L = 0.1\mu\text{m}$ for InP material), $d_D = 0.2\mu\text{m}$ ($D = \text{GaAs}$ material) (b) output simulation results (c) 1D-profile and (d) 3D-profile of the light propagation in the model design by using OptiFDTD@optiwave commercial software (KMITL License).

In Figure 2.11 the simulation results in two nested microring coupled to multilayer grating. The output results are sharpness at the resonant peak as shown in figure 2.11(b).

Chapter 3

Research methodology

In this thesis, I use the OptiFDTD@Optiwave commercial software (KMITL License) for simulation.

3.1 Mathematical Model

I consider an azimuthally symmetric structure as illustrated in Figure. 3.1. The nested microring resonator consists of a material with refractive index n_H and n_L for higher and lower layers, respectively. All the electromagnetic field components can be expressed by the components of the electrical and magnetic fields [25], which satisfy the Helmholtz equation;

$$\left[\frac{1}{\rho} \frac{\partial}{\partial \rho} \left(\rho \frac{\partial}{\partial \rho} \right) + \frac{1}{\rho^2} \frac{\partial^2}{\partial \theta^2} + k_0^2 n^2(\rho) + \frac{\partial^2}{\partial z^2} \right] E_z = 0 \quad (3.1)$$

where ρ , z and θ are the radial, axial, and azimuthal coordinates, respectively, and k_0 is the wavenumber in vacuum. The refractive index $n(\rho)$ equals either n_H or n_L depending on the radius ρ . Assumption of the dependence of the fields on the coordinates can be separated, the radial part of the fields (either H_z or E_z), $R_{H,E}$, must satisfy the Bessel equation;

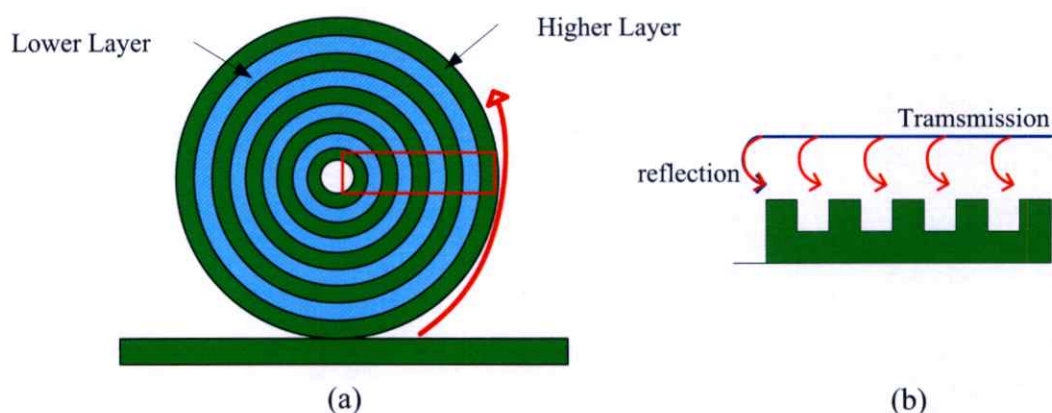


Figure 3.1. (a) Schematic of the nested microring resonator in InGaAsP/InP for higher and lower layers, respectively and (b) diagram of transmission and reflection light pulse.

$$\rho^2 \frac{\partial^2 R_E}{\partial \rho^2} + \rho \frac{\partial R_E}{\partial \rho} + [(k^2(\rho) - \beta^2)\rho^2 - m] R_E = 0 \quad (3.2)$$

where $k(\rho) = k_0 \cdot n(\rho)$, m is an integer and β is the z component of the wave vector. The solutions of (3.2) are a superposition of the m th-order Bessel functions of the first and second kind;

$$E_z = \left[A \cdot J_m(\sqrt{k_j^2 - \beta^2}\rho) + B \cdot Y_m(\sqrt{k_j^2 - \beta^2}\rho) \right] \cos(\beta \cdot z + \varphi) \cdot \exp(im\theta) \quad (3.3)$$

where A , B , C , and D are independent coefficients and k_j is the material wavenumber in the j th layer. The other four components of the electric and magnetic fields can be readily derived from eq. (3.3).

The parallel component of the fields— E_z , and E_θ —must be continuous at the interfaces separating successive layers. This requirement can be written in form of a transfer matrix, connecting the amplitude vector $[A \ B \ C \ D]$ in the j th and $j+1$ layers;

$$\begin{pmatrix} A_{j+1} \\ B_{j+1} \\ C_{j+1} \\ D_{j+1} \end{pmatrix} = \tilde{M}_{j+1}^{-1}(\rho_{j+1}) \cdot \tilde{M}_j(\rho_j) \cdot \begin{pmatrix} A_j \\ B_j \\ C_j \\ D_j \end{pmatrix} \quad (3.4)$$

$$\tilde{M}_j = \begin{pmatrix} J(\gamma_j \rho) & Y(\gamma_j \rho) & 0 & 0 \\ \frac{n_j^2}{\gamma_j} J'(\gamma_j \rho) & \frac{n_j^2}{\gamma_j} Y'(\gamma_j \rho) & \frac{m\beta}{\rho\omega\epsilon_0\gamma_j^2} J(\gamma_j \rho) & \frac{m\beta}{\rho\omega\epsilon_0\gamma_j^2} Y(\gamma_j \rho) \\ 0 & 0 & J(\gamma_j \rho) & Y(\gamma_j \rho) \\ \frac{m\beta}{\rho\omega\mu\gamma_j^2} J(\gamma_j \rho) & \frac{m\beta}{\rho\omega\mu\gamma_j^2} Y(\gamma_j \rho) & \frac{1}{\gamma_j} J'(\gamma_j \rho) & \frac{1}{\gamma_j} Y'(\gamma_j \rho) \end{pmatrix} \quad (3.5)$$

where ε and μ are the dielectric and magnetic susceptibilities, ω is the optical angular frequency, $\gamma_j = \sqrt{k_j^2 - \beta^2}$, and the primes indicate derivative with respect to the function argument.

In the above-mentioned limit, each polarization component can be described by two coefficients in each layer: A_j and B_j for TM and C_j and D_j for TE. For each polarization, the boundary conditions at the interfaces between successive layers can be represented similarly to (3.4) using simplified 2×2 matrices

$$\tilde{M}_j^{TM} = \begin{pmatrix} J(\gamma_j \rho) & Y(\gamma_j \rho) \\ \frac{n_j^2}{\gamma_j} J'(\gamma_j \rho) & \frac{n_j^2}{\gamma_j} Y'(\gamma_j \rho) \end{pmatrix} \quad (3.6)$$

$$\tilde{M}_j^{TE} = \begin{pmatrix} J(\gamma_j \rho) & Y(\gamma_j \rho) \\ \frac{1}{\gamma_j} J'(\gamma_j \rho) & \frac{1}{\gamma_j} Y'(\gamma_j \rho) \end{pmatrix}$$

Using (3.4) and the matrices (3.6), the field components can be “propagated” from the external layers to the inner layers. I use the finiteness of the field at $\rho = 0$ so that $B_1 = D_1 = 0$. The second boundary condition is no inward propagating field beyond the last layer, so that $B_{N+1} = -iA_{N+1}$ for TM and $C_{N+1} = -iD_{N+1}$ for TE, where N is the number of layers.

3.2 Optiwave@FDTD Testing

In Figure. 3.2, the schematic diagram of a microring resonator includes gap coupling effect. The resonant peaks are depended on the gap coupling (g), waveguide width (w) as shown in Figure. 3.2.

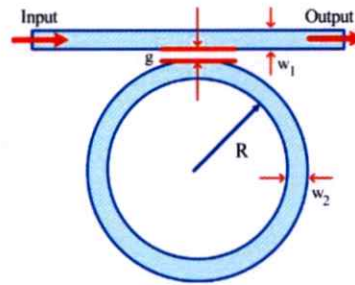


Figure 3.2 Scheme of microring resonator. g : gap coupling, w_i : waveguide width, R : microring resonator radius $4.7\mu\text{m}$

The transmission function of microring resonator is

$$T = \frac{|j(\omega - \omega_0)t + (\Gamma + R - 1)/2|^2}{|j(\omega - \omega_0)t + (\Gamma - R + 1)/2|^2} \quad (3.7)$$

where $t = L/v_g$ is the round-trip propagation time depending on the group velocity of the microring resonator. $L = 2\pi R$, Γ is microring loss. R is microring radius.

All numerical simulations in this paper I used are OptiFDTD software with Gaussian modulated continuous wave input pulse as;

$$E(t) = E_0 e^{\left[-\frac{(t-t_0)^2}{2T^2}\right]} \cdot \sin(\omega t). \quad (3.8)$$

where E_0 is field amplitude. t_0 is the time offset, T is the pulse width. $\omega = (2\pi/\lambda)c$ is the frequency of the input wave. λ is the wavelength input field and c is the velocity of light.

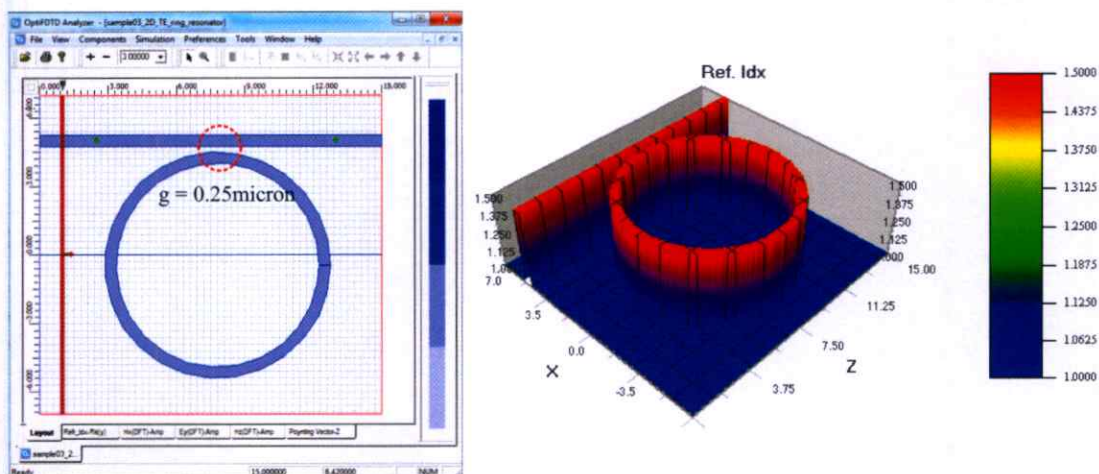


Figure 3.3 The model of microring for OptiFDTD test.

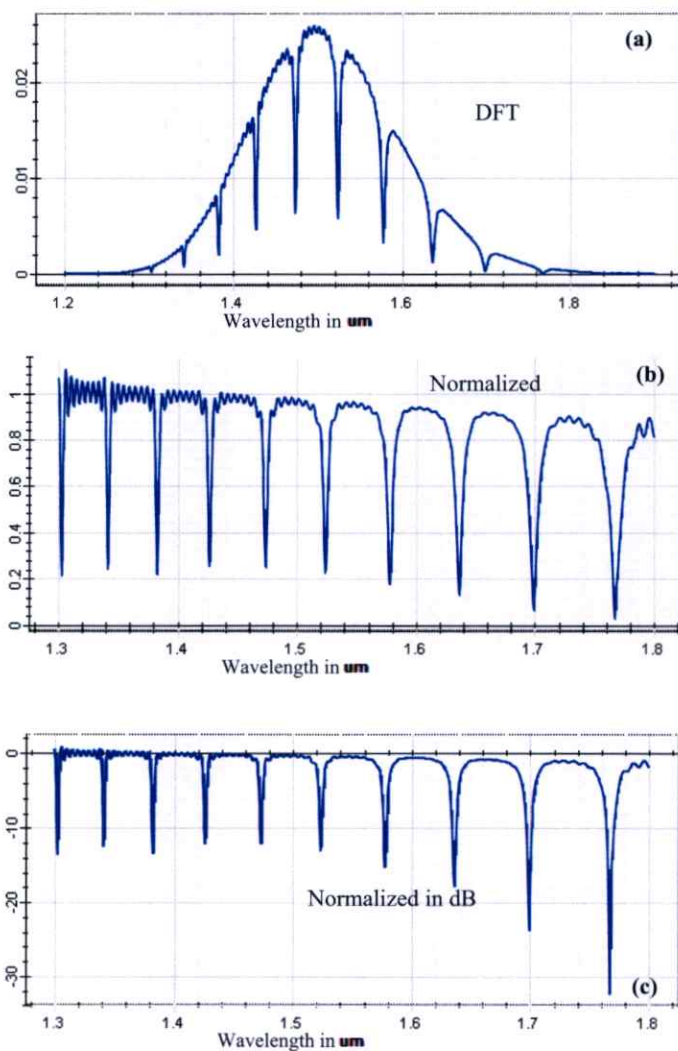


Figure 3.4 The simulation results of microring for OptiFDTD commercial software test.

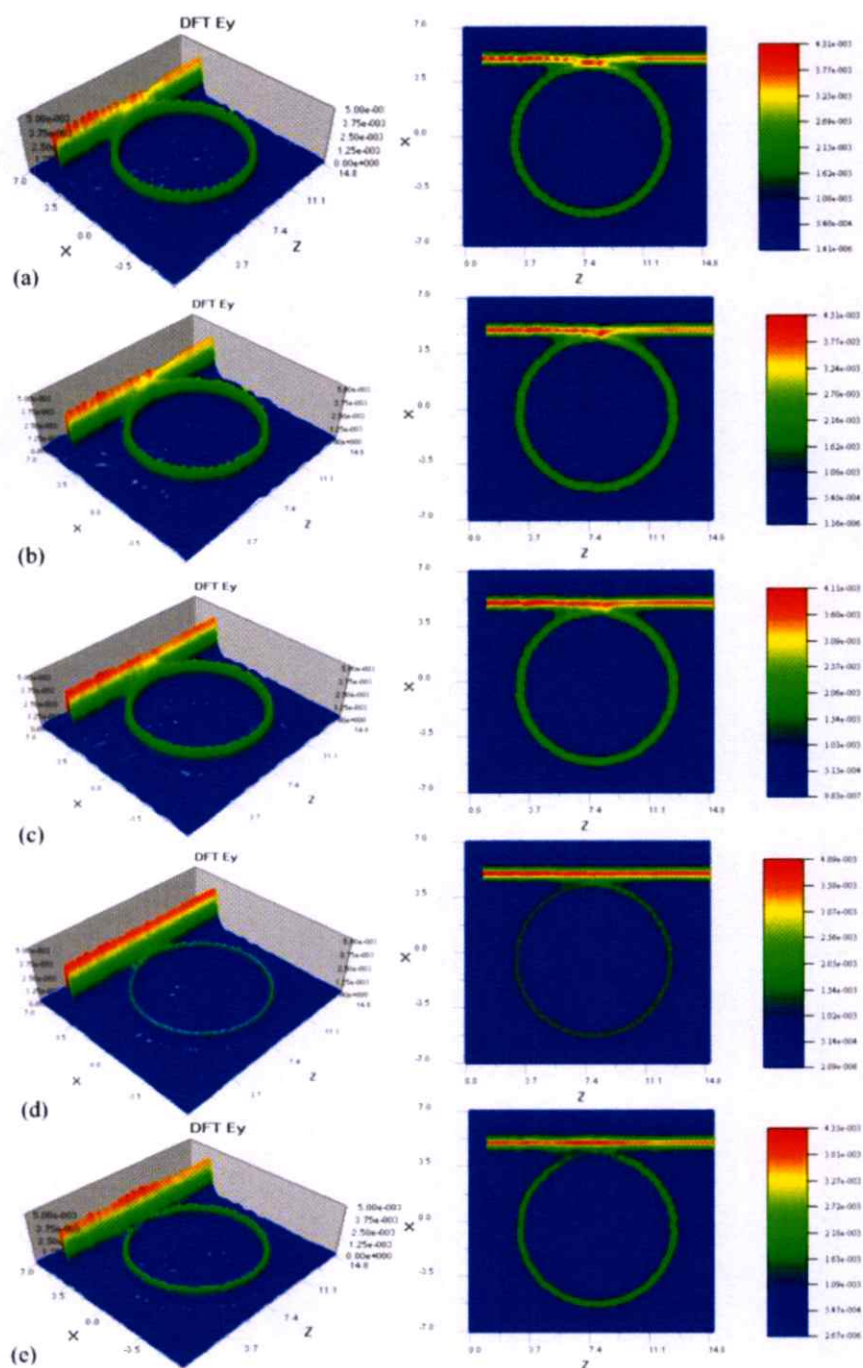


Figure 3.5 Simulation results of resonances peak in 3D view (first column) and 2D view (second column) by using OptiFDTD where (a) $w_1 = w_2 = 500\text{nm}$, $g = 0$, (b) $w_1 = w_2 = 500\text{nm}$, $g = 40\text{nm}$, (c) $w_1 = w_2 = 500\text{nm}$, $g = 120\text{nm}$, (d) $w_1 = w_2 = 500\text{nm}$, $g = 300\text{nm}$, and (e) $w_1 = 350\text{nm}$, $w_2 = 500\text{nm}$, $g = 40\text{nm}$

When the resonant peak is generated by changing the gap coupling effect of single microring resonator, I found that the resonant peak are shifted when the gap coupling increases as shown in Figures. 3-4.

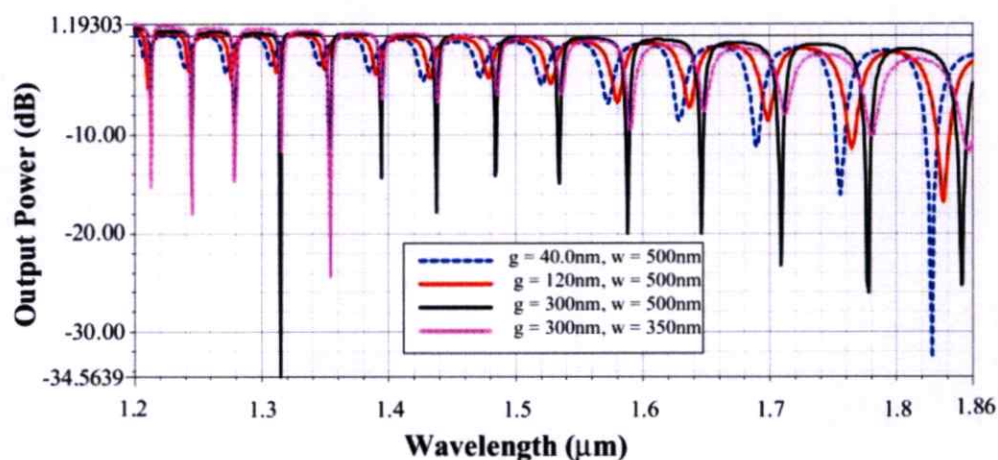


Figure 3.6 Output resonances of single microring resonator for very gap coupling.

For the $g = 300\text{nm}$, $w_1 = w_2 = 500\text{nm}$, the resonance is critical because the input light passes through the bus waveguide more than entrance to ring waveguide that can confirm as shown in Fig. 3.5 where (a) $w_1 = w_2 = 500\text{nm}$, $g = 0$, (b) $w_1 = w_2 = 500\text{nm}$, $g = 40\text{nm}$, (c) $w_1 = w_2 = 500\text{nm}$, $g = 120\text{nm}$, (d) $w_1 = w_2 = 500\text{nm}$, $g = 300\text{nm}$, and (e) $w_1 = 350\text{nm}$, $w_2 = 500\text{nm}$, $g = 40\text{nm}$, the off-resonance is occurred in Figure. 3.5(d).

Chapter 4

Results and Discussion

4.1 Transmission Characteristics of Optical Pulse in Nested Nonlinear Microring Resonators and Gratings

In this section, the optical trapping tool generation method is proposed, where the nanoparticle trapping model is analyzed and approached. The system is consisted of two-defect grating incorporating to nested nonlinear microring resonator (NMR) and the uniform grating at the output port as shown in Figure. 4.1

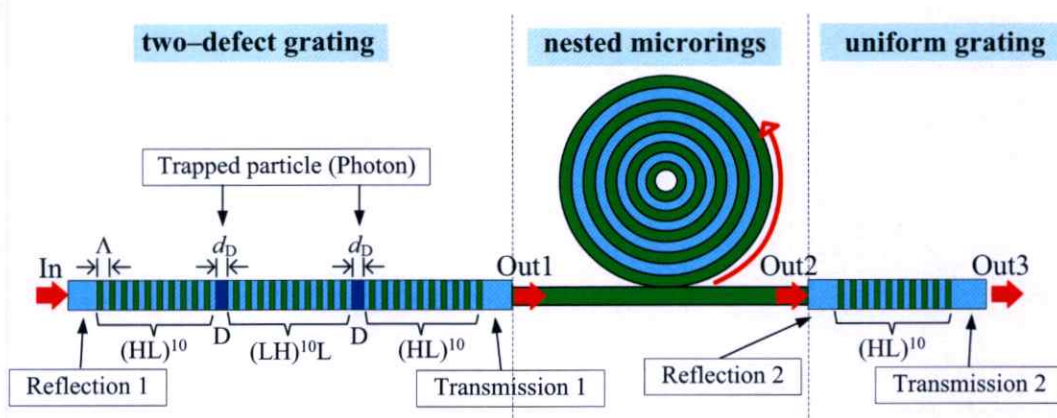


Figure 4.1 Schematic diagram of transmission behaviors of light in nested nonlinear microring resonator and gratings, where $\Lambda = 0.2\mu\text{m}$ ($H = 0.1\mu\text{m}$ for InGaAsP material, $L = 0.1\mu\text{m}$ for InP material), $d_D = 0.2\mu\text{m}$ ($D = \text{GaAs}$ material)

The simulation parameters are fixed by the refractive index of waveguide, $n_H = 3.51$ for InGaAsP material, the waveguide width and high is fixed to be $1\mu\text{m} \times 1\mu\text{m}$.

The radii of nested nonlinear microring are 1.1, 1.7, 2.3, 2.9, and 3.1 μm for high layers, respectively, for InGaAsP material ($n_H = 3.51$). The lower layer is used the InP material with the refractive index, $n_L = 3.22$, where the nonlinear refractive index is $2.2 \times 10^{-13} \text{ m}^2\text{W}^{-1}$ (InGaAsP/InP). The simulation results are used the finite difference time domain (FDTD) Optiwave@OptiFDTD which is a commercial software program, however, the device parameters are chosen closely to the practical fabrication parameters.

4.1.1 Two-defect Grating

The transmission coefficients of the two-defect grating in the symmetric structure $(\text{HL})^{10}\text{D}(\text{LH})^{10}\text{LD}(\text{HL})^{10}$ and the uniform structure $(\text{HL})^{10}$ are close to 1 and 1.6, respectively, as shown in Figure. 4.2. For the transmission light pulse versus the frequency of two-defect grating (red curve) and uniform grating (blue curve), I found that the two optical tweezers are occurred when the two-defect grating adding with the full-width half maximum is 29.07THz. The spectrum of uniform grating is stoped band in the frequency range 185THz to 210THz.

4.1.2 Nested Nonlinear Microring Resonator (NMR)

The transfer function of nested nonlinear microring resonator is resonant at 197.07THz (FWHM = 100GHz) as shown in Figure. 4.3 The Q -factor ($\Delta f/f_0$) of MMR is 1970.7 and the resonant peak output power is 21.34 dBm at 197.07THz. The dynamic pulse propagation results shown in Figure. 4.4 represents the generalized the light pulse traveling through the MMR design model in TE mode by using continuous wave (cw) Gaussian pulse of Optiwave@FDTD commercial software. In the FDTD simulation, a femto-second pulse with the cw Gaussian waveform is launched into waveguide at

In-port, the field inside the MMR cavity at points 1, 2, 3, and 4 the output intensity field in the frequency domain (FD). I found that the confinement of intensity fields at points 1 and 4 are strength more than intensity fields at points 2 and 3, respectively, as shown in Figure. 4.4 (c)–(f). This is because the intensity field at points 1 and 4 is closed to straight waveguide that the optical intensities are coupled in this region. The optical manipulated is strong. In Out-port, I can see the peak sharpness at 197.07THz in frequency domain.

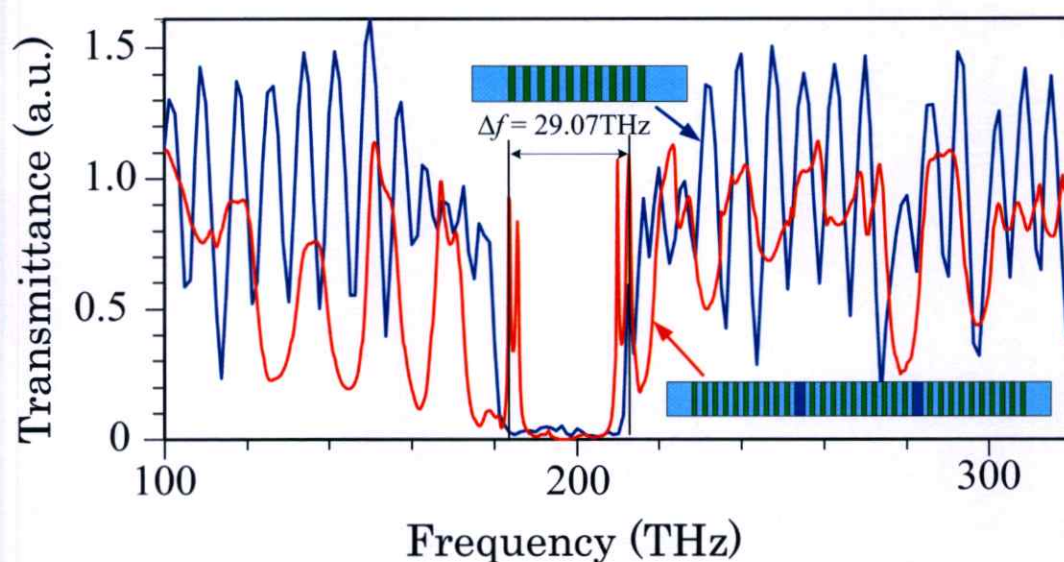


Figure 4.2 Shows the transmittance of two-defect multilayer and uniform grating, where two optical tweezers are occurring in two-defect multilayer and seen

In Figure. 4.5, the output intensity of NMR in Figure. 4.4 (h) is converted into the output power in dBm units, which is found that the resonant peak is occurred at 197.07THz with FWHM 123.57GHz (see inset Figure. 4.2) The output of optical tweezer is occurred within the frequency range from 201.80THz to 202.60THz. The free-spectral range (FSR) is 465.30GHz, which can be used to form the optical trapping tool for particle trapping.

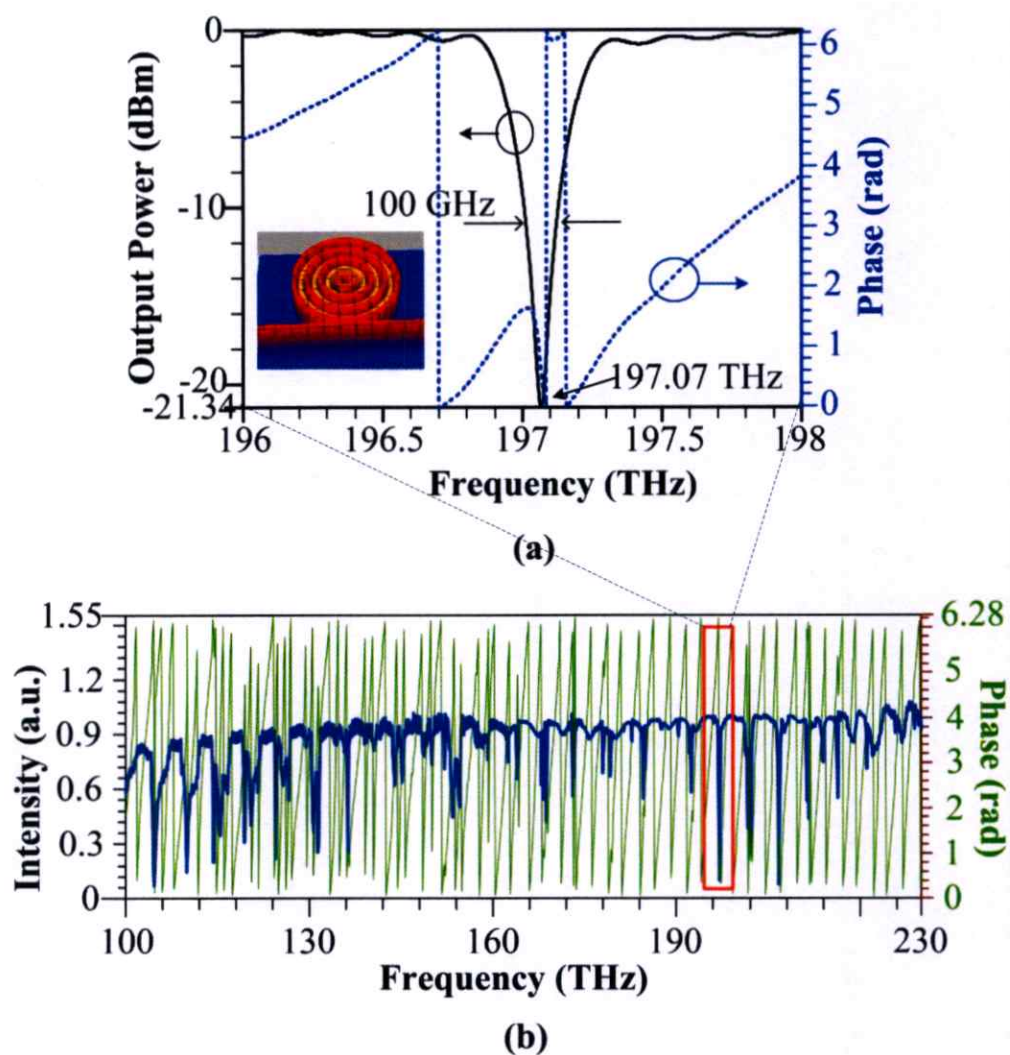


Figure 4.3 Shows the transfer function of transmission behavior light of nested nonlinear microring resonator

4.1.3 Transmission Behaviors of Light

The velocity of transmission light pulse passing through the second output (out2) at 187.5THz is 4.245×10^6 m/s, which is faster than the first output (out1), because the light pulse is delayed when it is passing through the two-defect grating, in which the particle(photon) can be trapped within the defect layers. On the other hand, the velocity of transmission light pulse through the first output (out1) at

214.3THz – 230.8THz is 3.003×10^6 m/s, which is faster as the second output (out2) that the light pulse propagate is slowly because the transmission behavior of light is filtered again when it is passing through the uniform grating output. For instance, the propagation velocity of light pulse can be determined locally, and it is often implicitly assumed by the group velocity ($v_{gr} = d\omega/dk$) [54]. The trapping region is broadening within range from 180 – 210 THz. In Figure. 4.6, the output intensity is detected in frequency domain at positions out1, out2, and out3 as shown in Figure. 4.4, where the red shift is seen at the about 175 THz in frequency domain, which is shifted from 175.2496THz to 175.0791THz and 175.0365THz, respectively. On the other hand, the blue shift is occurred at about 177THz.

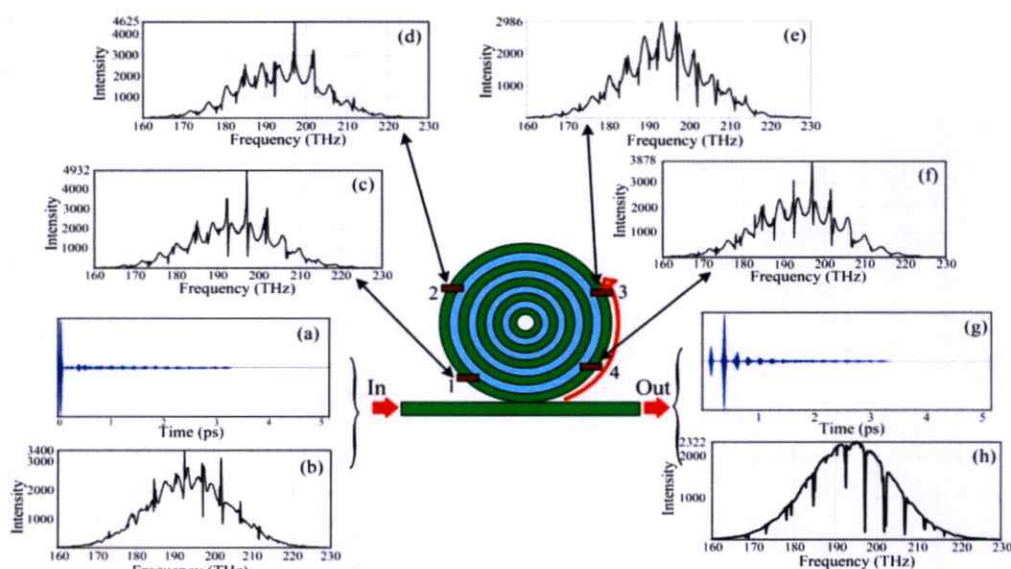


Figure 4.4 The transmission behaviors of light pulses in the nested nonlinear microring resonators, where (a) E -field of the input in time domain, and (b) the intensity in frequency domain, (c) – (f) the intensity in frequency domain at position 1, 2, 3, and 4, respectively. (g) E -field of the output in time domain, and (h) the intensity in frequency domain

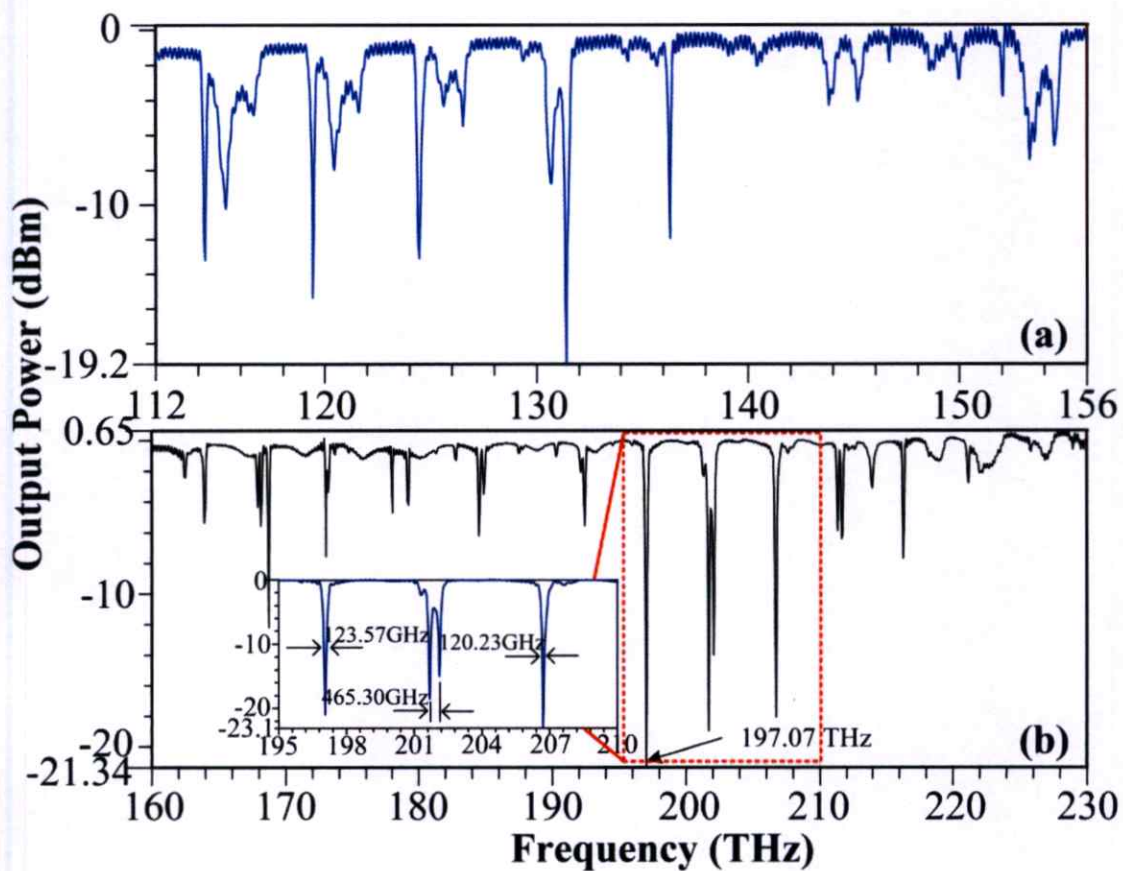


Figure 4.5 The output power of the output port of the transmission light pulse in frequency domain range, where (a) 112 – 156 THz and (b) 160 – 230 THz with frequency $f = 197.07$ THz, which is closest to a resonant mode of the nested nonlinear microring resonator (see Figure. 4.4).

The normalized trapping tool transmission intensity and wavelength are plotted in Figure. 4.7, which is confirmed that the optical tweezers are generated within the wavelength range from 214.3THz – 230.8THz as shown in Figure. 4.7(a)–(c), therefore, the resonant transmission at the center wavelength is neglected by the uniform multilayer with nested nonlinear microring resonators incorporating that design for 187.5THz filter signal out, which can be claimed as the trapping band(stop-band) for particle trapping applications.

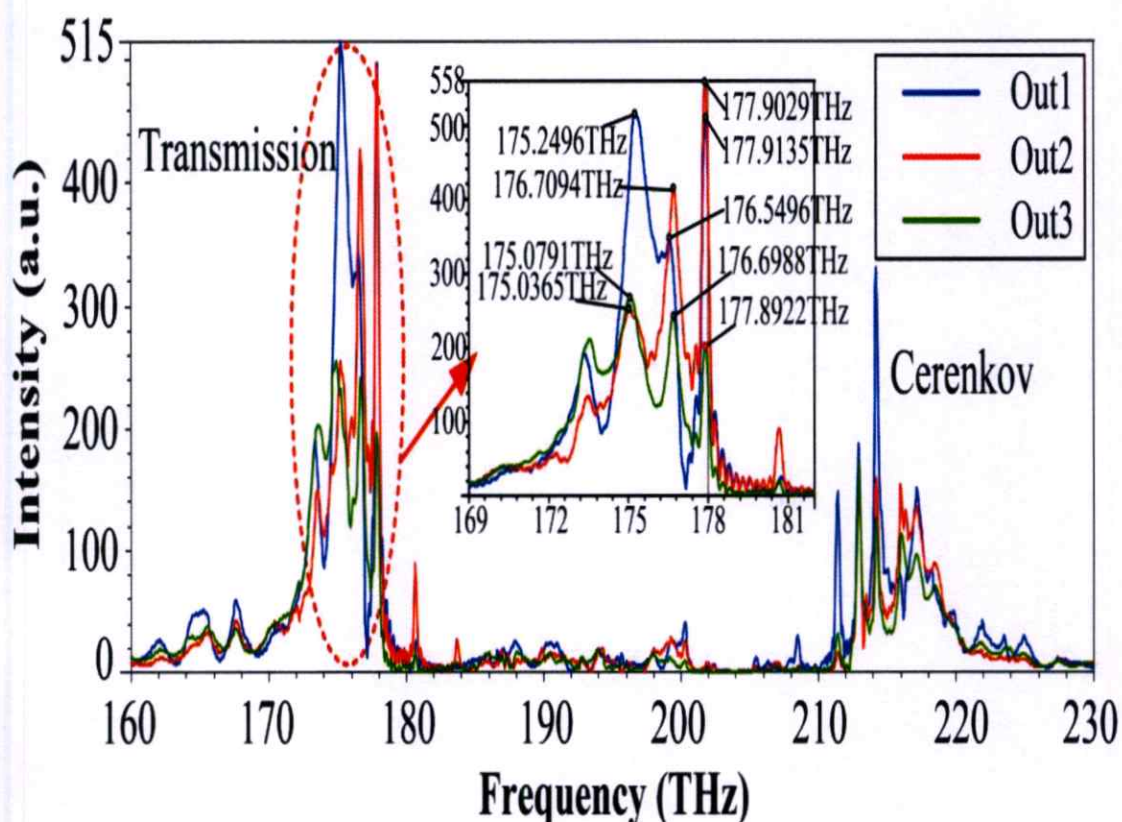


Figure 4.6 The output intensity is detected in frequency domain at the point out1, out2, and out3 in Figure. 4.1 (Inset) the output intensity of nested nonlinear microring resonator and gratings, which is range from 169THz – 181THz

4.1.4 Red-shifted and Blue-shifted Čerenkov Radiation

The Čerenkov radiation of light in nested nonlinear microring resonators and gratings are occurred, which is shown that the continuously blue-shifted is occurred at the center frequency 215 THz, while the red-shifted is seen at 175 THz, as shown in Figure. 4.6, which means that the red-shifted and blue-shifted (Čerenkov radiation) of the first and second transmission behaviors of light pulse (Gaussian pulse) with the input wavelength center at 193.5THz are seen and confirmed, respectively.

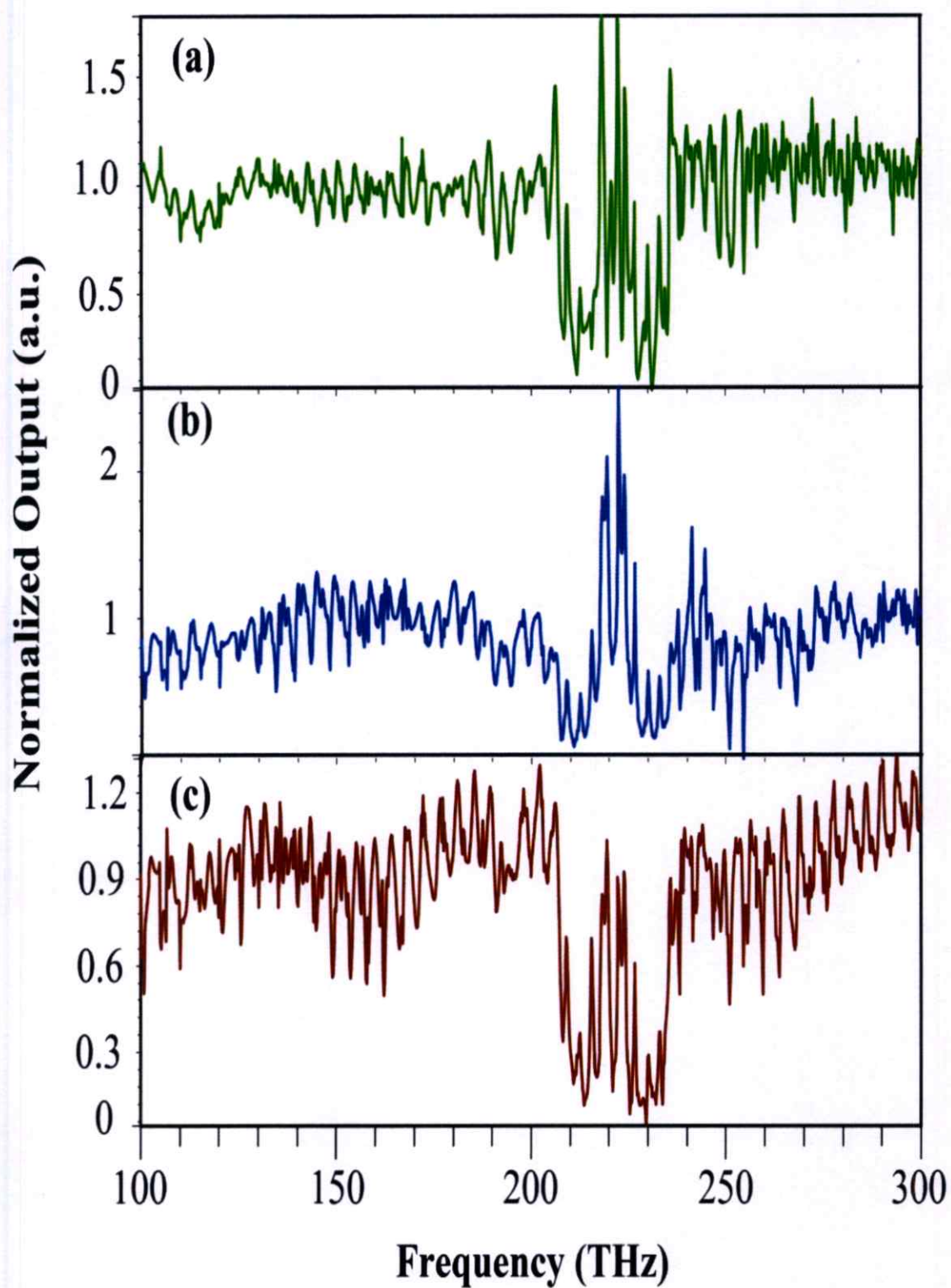


Figure 4.7 Shows the relationship between normalized intensity output and input, where (a) out1, (b) out2, and (c) out3.

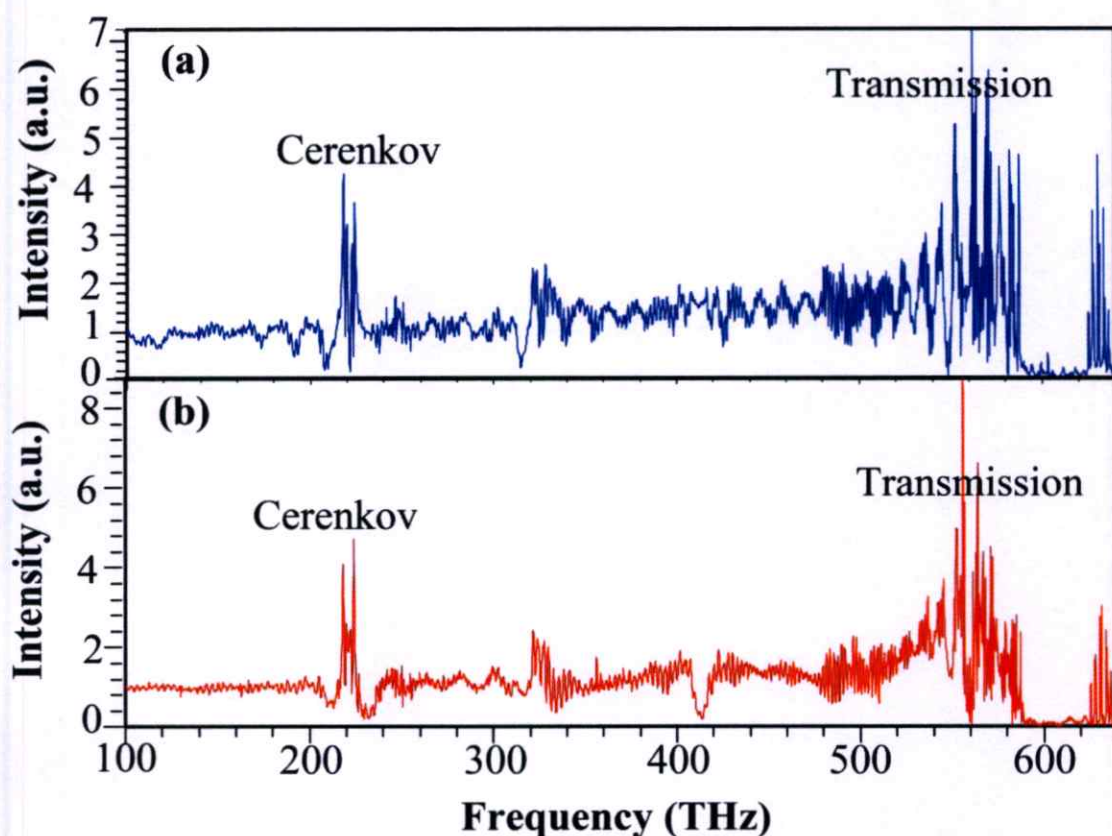


Figure 4.8 Shows the FFT results of two-defect modes, where (a) the first and (b) the second defect modes for two-defect grating.

4.2 Doppler Shift Velocimetry Using Two Point Probe Nested-microring Resonators

Figure 4.9 illustrates the principle of the proposed Doppler frequency shift velocimeter for 2D velocity measurement. The input cw Gaussian light pulse at the center frequency 193.55THz has 1.439nW power modal index is (3.3012, 0), time offset is 5×10^{-14} s, half width is 1.4×10^{-14} s, respectively. The input light pulse is launched into the bus waveguide width, w_2 , with the incident angle 30° . The incident

light pulse from the bus waveguide is propagated to the first nested-microring with the gap coupling equal zero. The structure in each nested-microring includes the multilayer of upper and lower layers with the radii $R_1 - R_7$ (see Fig.8(a)). The light pulse is circulated in the first nested-microring called "Reference" signal detected by "sensor 1". The multilayer in the first nested-microring has width identical equal to w_1 . The transmission or output light intensity is measured by "Out1 (Figure 4.9 (a))" or "Out2 (Figure 4.9 (b))". Here, the phase of transmit and circulate intensity of the first nested-microring is shifted so that the phase difference become π rad. The output intensity from Out1 (Figure 4.9 (a)) or Out2 (Figure 4.9 (b)) is launched into the second nested-microring with light coupled gap equal to zero. The light intensity is circulated in the second nested-microring called "Sensing" signal detected by "Sensor 2". The multilayer in the second nested-microring has been identical to the first. The transmission or output light intensity is measured by "Out2 (Figure 4.9 (a))" or "Out3 (Figure 4.9 (b))". Here, the phase of transmit and circulate intensity of the second nested-microring is shifted so that the phase difference become π rad as well. The beat frequency of the beat signal produced by the interference between the circulate intensity of "Reference" and "Sensing" signals, and between the "Out1" and "Out2" in Figure 4.9 (a) or "Out2" and "Out3" in Figure 4.9 (b) It was measured the Doppler frequency shift velocimeter.

Similarly. in Figure 4.9 (b) the incident light pulse from the bus waveguide is propagated to the two-defect grating. Before going to the first nested-microring is measuring at the "Out1" as input source.

When the two nested-microrings is usually explained as the path length change is induced. However, it is equally valid to consider the light intensity circulated in two nested-microrings as being due to a frequency shift, Δf ,

experienced by the light interference as it is reflected and transmitted between them. The beat frequency experiences are shifted in frequency as [16],

$$\Delta f = \frac{2fv}{c} \quad (1)$$

where v is the relative velocity between two nested-microrings, c is the speed of light (3×10^8 m/s) and f is the frequency of the cw Gaussian light (193.55THz).

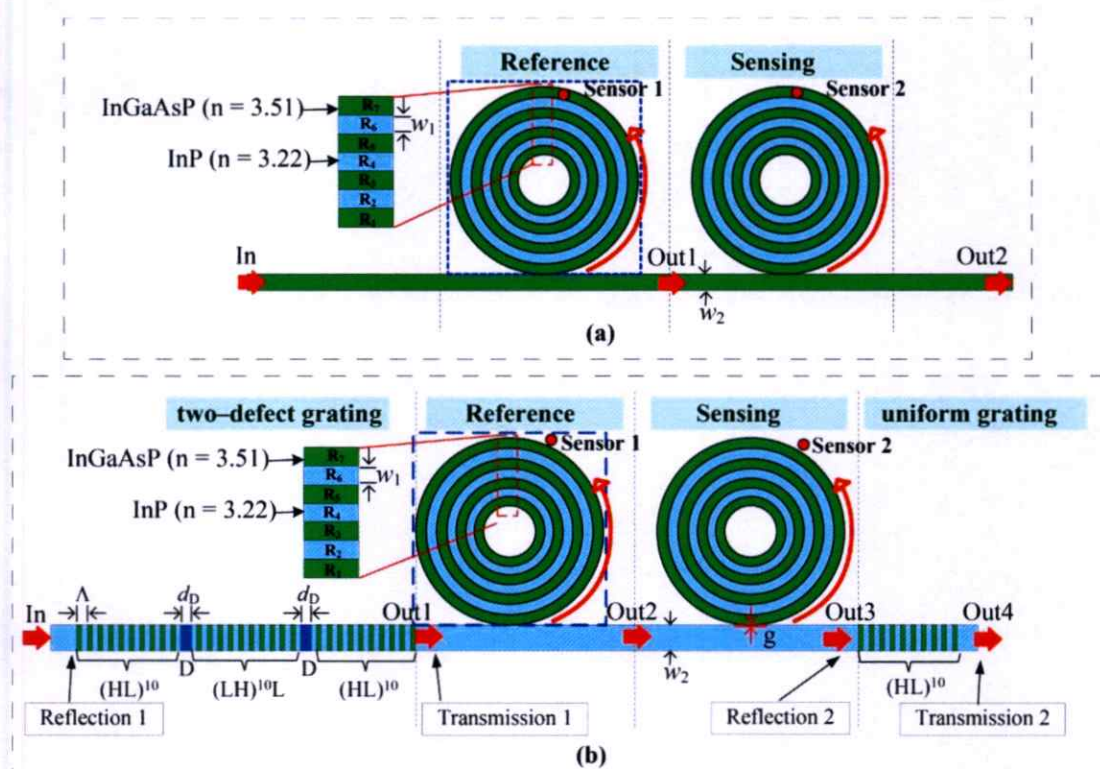


Figure. 4.9 Schematic diagram of the nested microring resonator (a) without gratings and (b) with gratings with sensors 1 (Reference signal) and sensor 2 (Sensing signal) for optical signal circulate detect, where Λ period grating, H is upper InGaAsP material layer, L is lower InP material layer, d_D is defect width for GaAs material, ($\Lambda = 0.2\mu\text{m}$, $H = 0.1\mu\text{m}$, $L = 0.1\mu\text{m}$, $d_D = 0.2\mu\text{m}$), g is gap coupling, w_1 and w_2 are nested microring resonator-and bus-width, respectively, $R_1, \dots, 7$ are radii of nested-microring resonators.

In this section, the optical Doppler frequency shift velocimeter is proposed. The system is consisted of nested nonlinear microring resonator (NMR) without and with the uniform grating as shown in Figure 4.9. The simulation parameters are fixed by the refractive index of waveguide, $n_H = 3.51$ for InGaAsP material, the waveguide width and height are fixed to be $0.5\mu\text{m} \times 0.5\mu\text{m}$. The radii of nested nonlinear microring are 1.0, 1.5, 2.0, 2.5, 3.0, 3.5, and $4.0\mu\text{m}$, respectively, for InGaAsP material ($n_H = 3.51$). The lower layer is used the InP material with the refractive index, $n_L = 3.22$, where the nonlinear refractive index is $2.2 \times 10^{-13} \text{ m}^2\text{W}^{-1}$ (InGaAsP/InP). The simulation results come from the finite difference time domain (FDTD) Optiwave@OptiFDTD (KMITL single license) which is a commercial software program, however, the device parameters are chosen closely to the practical fabrication parameters. The transmission coefficients of the two-defect grating in the symmetric structure $(\text{HL})^{10}\text{D}(\text{LH})^{10}\text{LD}(\text{HL})^{10}$ and the uniform structure $(\text{HL})^{10}$ are closed to 1 and 1.6, respectively [17]. Two optical tweezers are occurred when the two-defect grating adding with the full-width half maximum of 29.07THz. The spectrum of uniform grating is stop band in the frequency range from 185THz to 210THz.

4.2.1. Two Point Probe Doppler Velocimetry

The schematic diagram of two nested-microring resonators without gratings is proposed, as shown in Figure. 4.9 (a). The layer width, w_1 , of nested-microring resonator is fixed at $0.5\mu\text{m}$. The interference intensity of light pulse is occurred through the circulate intensity both in reflection and transmission [18]. The beat frequency of the beat signal produced by the interference between the circulate intensity of "Reference" and "Sensing" signals, and between the "Out1" and "Out2"

for Doppler frequency shift velocimeter was measured. The light intensity at the center of two nested-microrings is called whispering gallery mode [19].

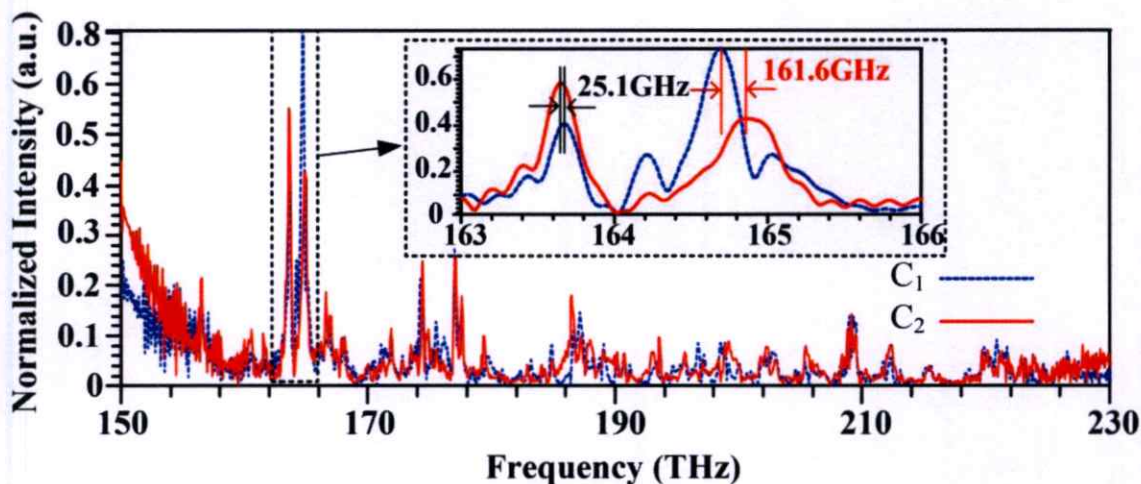


Figure. 4.10 Shows the WGMs of light pulses at the center, where (C1) and second (C2) are the first and second nested-microring resonators without gratings, respectively.

Figure. 4.10 shows the whispering gallery modes (WGMs) of the cw Gaussian light pulse as a function of the frequency passes through the center of first nested-microring resonator (blue curve) and second nested-microring resonator (red curve) without gratings. I found that the phase of two WGM of the first nested-microring is shifted so that the phase difference becomes $\pi/2$ rad with the second. The frequency shift is equal to 25.1GHz and 161.6GHz, the relative velocity is 1.95×10^4 m/s and 1.25×10^5 m/s, respectively.

In Figure. 4.11, the optical intensity transmit and circulate has phase shift π radian. The free-spectral range (FSR) of the optical intensity transmission and circulation in the first and second nested-microring resonator are 3.2777THz and 3.1563THz, respectively (see Figure 4.11 (a) and (b)). The FSR of second nested-

microring resonator is narrow more than the first nested-microring resonator because the optical reflected doubling or higher than once. The Doppler frequency shifts of the optical intensity are circulated in the first, and second nested-microring resonator at points ① and ② is 42.5GHz (3.29×10^4 m/s), ③ and ④ is 175.3GHz (1.36×10^5 m/s), ⑤ and ⑥ is 164.6GHz (1.28×10^5 m/s), ⑦ and ⑧ is 37.1GHz (2.88×10^4 m/s), (see inset Fig. 10).

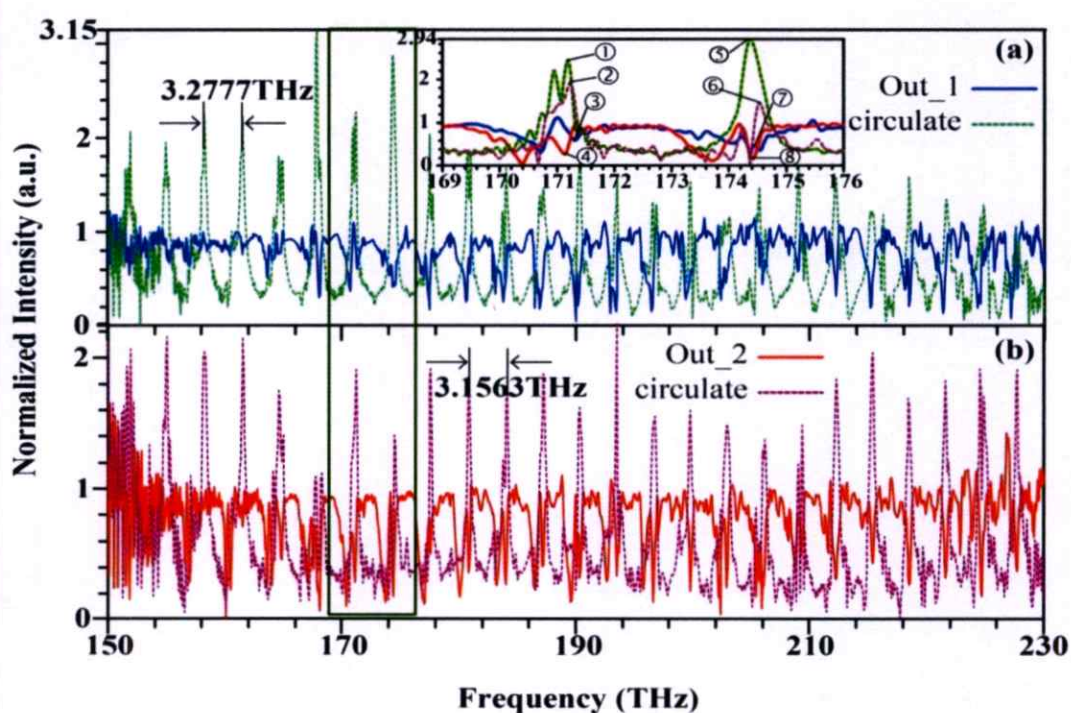


Figure. 4.11 The transmission (out) and circulation (circulate) of light intensity when propagate through (a) the first and (b) second nested microring resonators without gratings. (inset) ① the first circulate intensity 171.1908THz, ② the second circulate intensity 171.2333THz, ③ the first transmit intensity 171.3077THz, ④ the second transmit intensity 171.1324THz, ⑤ the first circulate intensity 174.3722THz, ⑥ the second circulate intensity 174.5368THz, ⑦ the first transmit intensity 174.4571THz, ⑧ the second transmit intensity 174.4200THz.

4.2.2 Two Wavelength Probe Doppler Velocimetry

The schematic diagram of two-nested-microring resonator with gratings is proposed, as shown in Figure 4.9 (b). The layer width, w_1 , of nested-microring resonator is fixed at $0.5\mu\text{m}$. The interference intensity of light pulse is occurred through the circulate intensity both in reflection and transmission. The beat frequency of the beat signal produced by the interference between the circulate intensity of “Reference” and “Sensing” signals, and between the “Out2” and “Out3” for Doppler frequency shift velocimeter was measured. The two-defect grating $(\text{HL})^{10}\text{D}(\text{LH})^{10}\text{LD}(\text{HL})^{10}$ at the input port has been enhanced the intensity signal before launching into the first nested-microring. The uniform grating $(\text{HL})^{10}$ at end of waveguide has been filtered light signal for manipulation or trapping tool use [17].

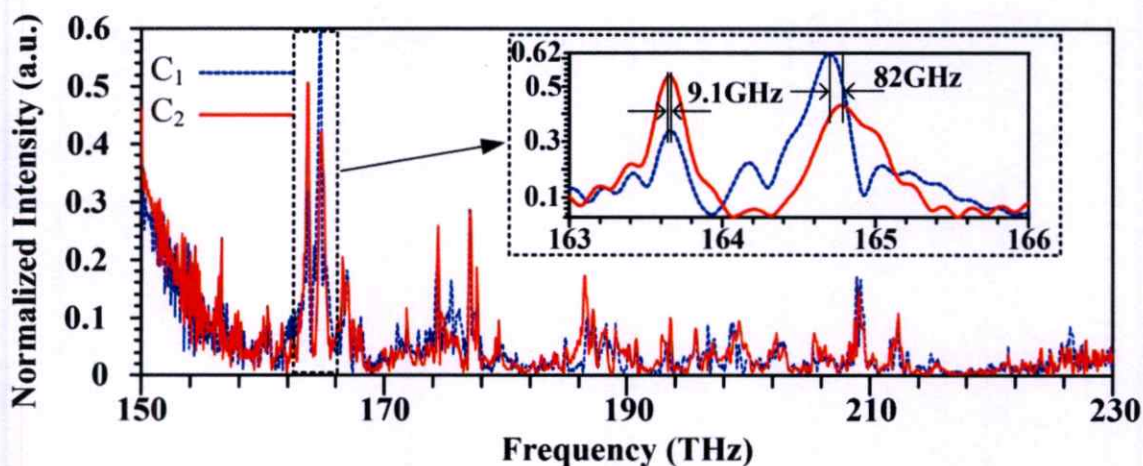


Figure. 4.12 The WGMs of light pulse detect at the center of first (C_1) and second (C_2) nested microring resonator with gratings.

Figure. 4.12 shows the whispering gallery modes (WGMs) of the cw Gaussian light intensity as a function of the frequency passes through the first nested-

microring resonator (blue curve) and second nested-microring resonator (red curve). I found that the phase of two WGM of the first nested-microring is shifted so that the phase difference becomes $\pi/2$ rad with the second. The frequency shift is equal to 9.1GHz (7.05×10^3 m/s) and 82GHz (6.35×10^4 m/s), respectively.

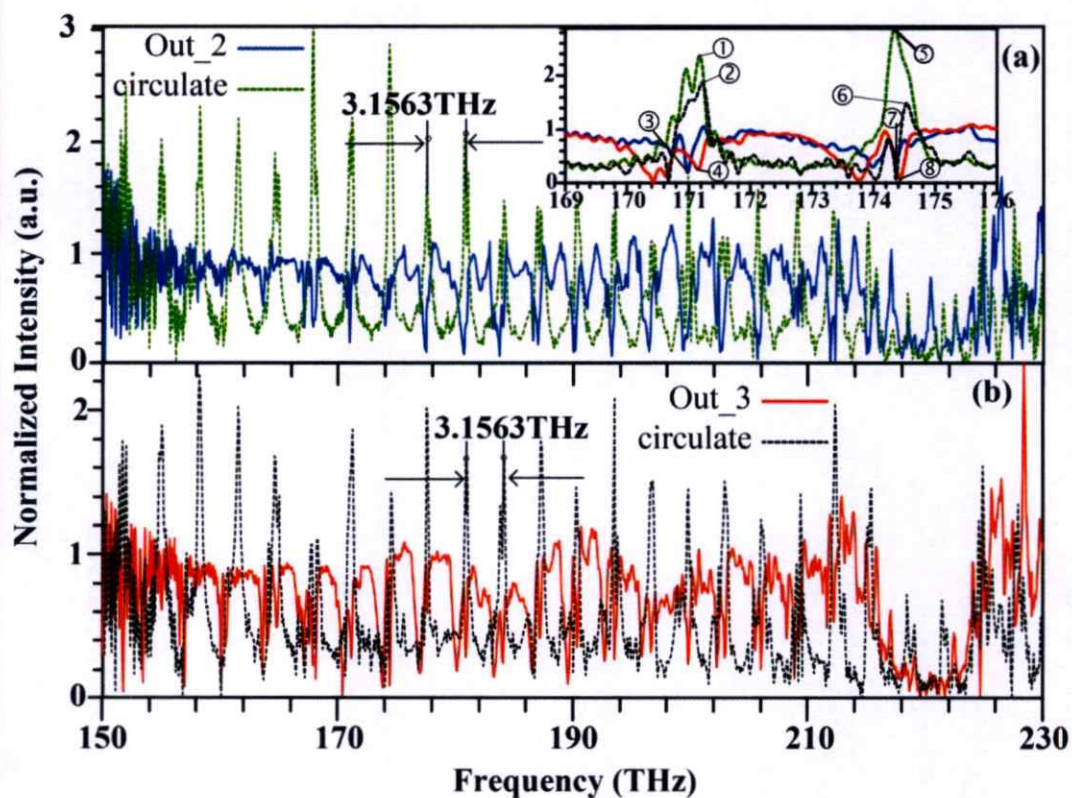


Figure. 4.13 The transmission (out) and circulation (circulate) of light intensity when propagate through (a) the first and (b) second nested microring resonators with gratings. (inset) ① the first circulate intensity 171.1802THz, ② the second circulate intensity 171.2280THz, ③ the first transmit intensity 170.9890THz, ④ the second transmit intensity 171.1536THz, ⑤ the first circulate intensity 174.3403THz, ⑥ the second circulate intensity 174.5368THz, ⑦ the first transmit intensity 174.3722THz, ⑧ the second transmit intensity 174.4359THz.

In Figure. 4.13, the optical transmit and circulate intensity has phase shift π radian. The free-spectral range (FSR) of the optical intensity transmission and circulation in the first and second nested-microring resonator is the same number at 3.1563THz both (see Figure 4.5 (a) and (b)). The optical intensity has been filtering again at the frequency 215THz – 225THz (FSR = 10THz). The Doppler frequency shifts of the optical intensity are circulated in the first, and second nested-microring resonator at points ① and ② is 47.8GHz (3.70×10^4 m/s), ③ and ④ is 164.6GHz (1.28×10^5 m/s), ⑤ and ⑥ is 196.5GHz (1.52×10^5 m/s), ⑦ and ⑧ is 63.7GHz (4.94×10^4 m/s), faster than previous (without gratings) about three times (see inset Figure 4.13).

4.2.3. Vary the Gap Coupling of Second-Nested Microring Resonator

In this section i have varied the gap coupling of the second nested-microring resonator. The gap coupling between bus waveguide and nested-microring has been influenced the light intensity scatter [21], reflection and transmission sensitivity [18] of the circulate fields.

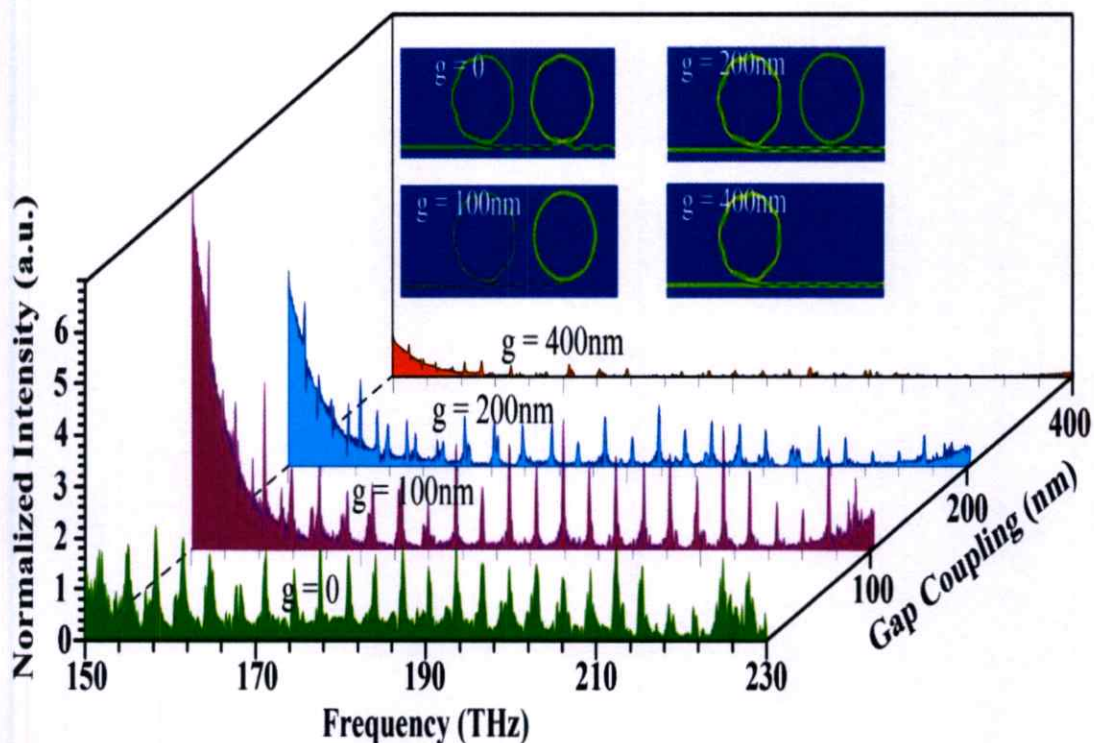


Figure. 4.14 The circulate intensity of the second nested-microring resonator with gratings for varies gap coupling. (inset) The profile of light intensity was traveling through the system design.

Figure. 4.14 shows the circulate intensity of the second nested-microring resonator with gratings as a function of the frequency for varies gap coupling in 0, 100nm, 200nm, and 400nm, respectively. I found that the second nested-microring is resonance for the gap coupling equals to 0 – 100nm and off-resonance for the gap coupling equal to 200nm – 400nm, respectively (see inset in Figure 4.14). This is because the light scatter are occurred for large gap coupling [22 – 23]. The range of filter is narrowed for the gap coupling equal to 100nm and 200nm, respectively.

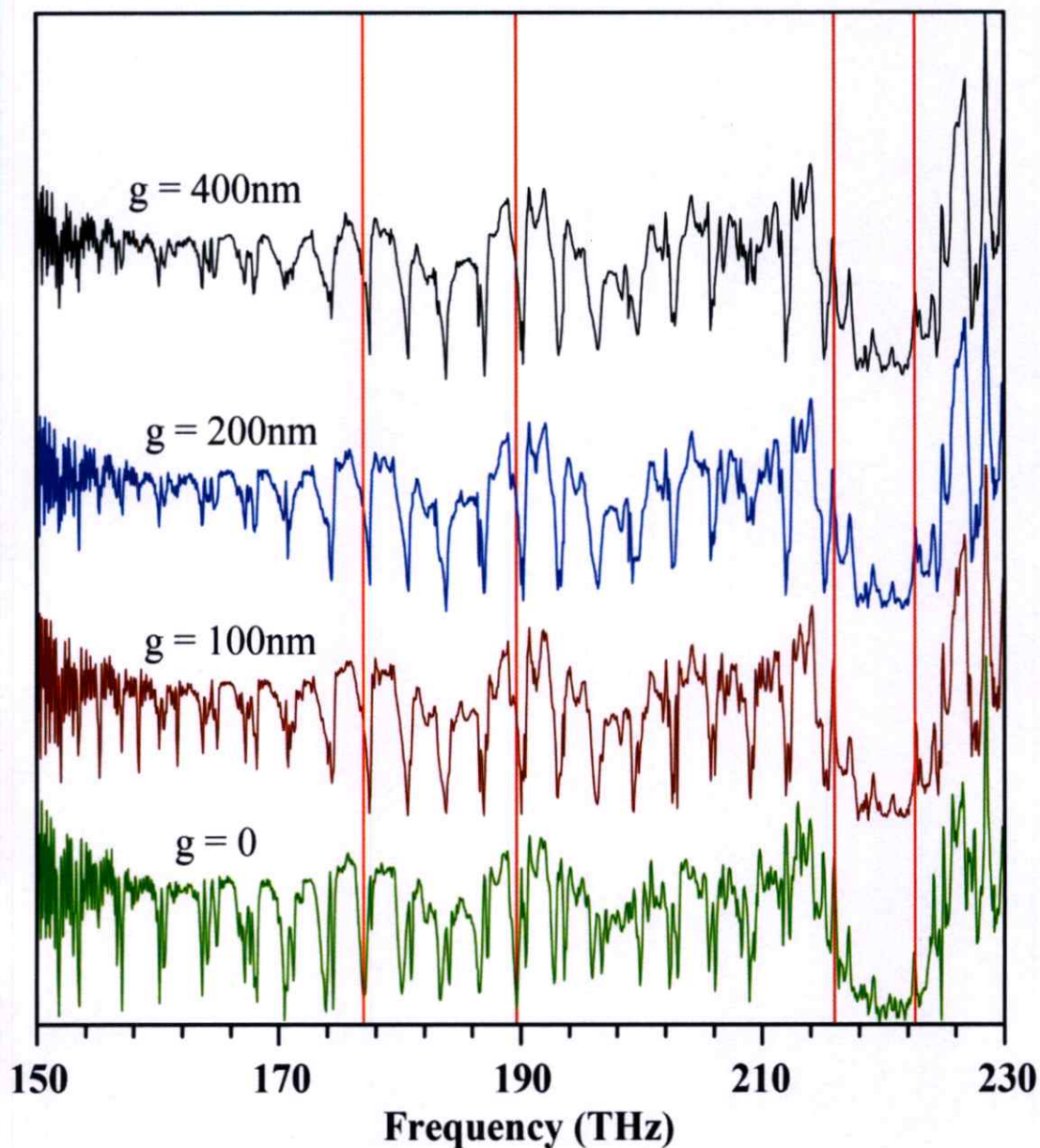


Figure 4.15 The transmit (output) intensities are detected at the second nested-microring resonator with gratings for varying gap coupling from 0 – 400nm.

Figure. 4.15 shows the transmit (output) intensities detected at the second nested-microring resonator with gratings for varying gap coupling from 0 to 400nm. I found that the transmission intensity has frequency shifted when the gap coupling between bus waveguide and the second nested-microring increase from 100nm to 400nm with beat frequency of 16.0GHz – 189.5GHz as shows in Figure. 4.16

In Figure 4.16 The transmit (output) intensities are measured at the first, and second nested-microring resonator with gratings for varied gap coupling of the second nested-microring resonator, for Figure 4.16 (a) $g = 0$, (b) $g = 100\text{nm}$, (c) $g = 200\text{nm}$, and (d) $g = 400\text{nm}$, respectively. The relative velocity of transmission (output) intensity for varied the gap coupling of the second nested-microring equal to 0, 100nm, 200nm, and 400nm are $1.44 \times 10^5 \text{ m/s}$ (185.9GHz), $1.73 \times 10^5 \text{ m/s}$ (223.1GHz), $1.56 \times 10^5 \text{ m/s}$ (201.8GHz), and $7.82 \times 10^4 \text{ m/s}$ (100.9GHz), respectively. The optical intensity is filtered at the frequency range 215THz – 221THz, because of the uniform at the end of optical waveguide design as shown in Figure 4.10 (b). The intensity light pulse has been decreased when gap coupling increases. The circulate intensity passes through the second nested-microring resonator with gratings for varies gap coupling as shown in Figure 4.17 (a) $g = 0$, (b) $g = 100\text{nm}$, (c) $g = 200\text{nm}$, and (d) $g = 400\text{nm}$, respectively. The relative velocity of circulation intensity for varied the gap coupling of the second nested-microring equal to 0, 100nm, 200nm, and 400nm are $4.12 \times 10^4 \text{ m/s}$ (53.1GHz), $1.28 \times 10^5 \text{ m/s}$ (165.5GHz), $1.18 \times 10^5 \text{ m/s}$ (152.0GHz), and $1.20 \times 10^4 \text{ m/s}$ (15.5GHz), respectively.

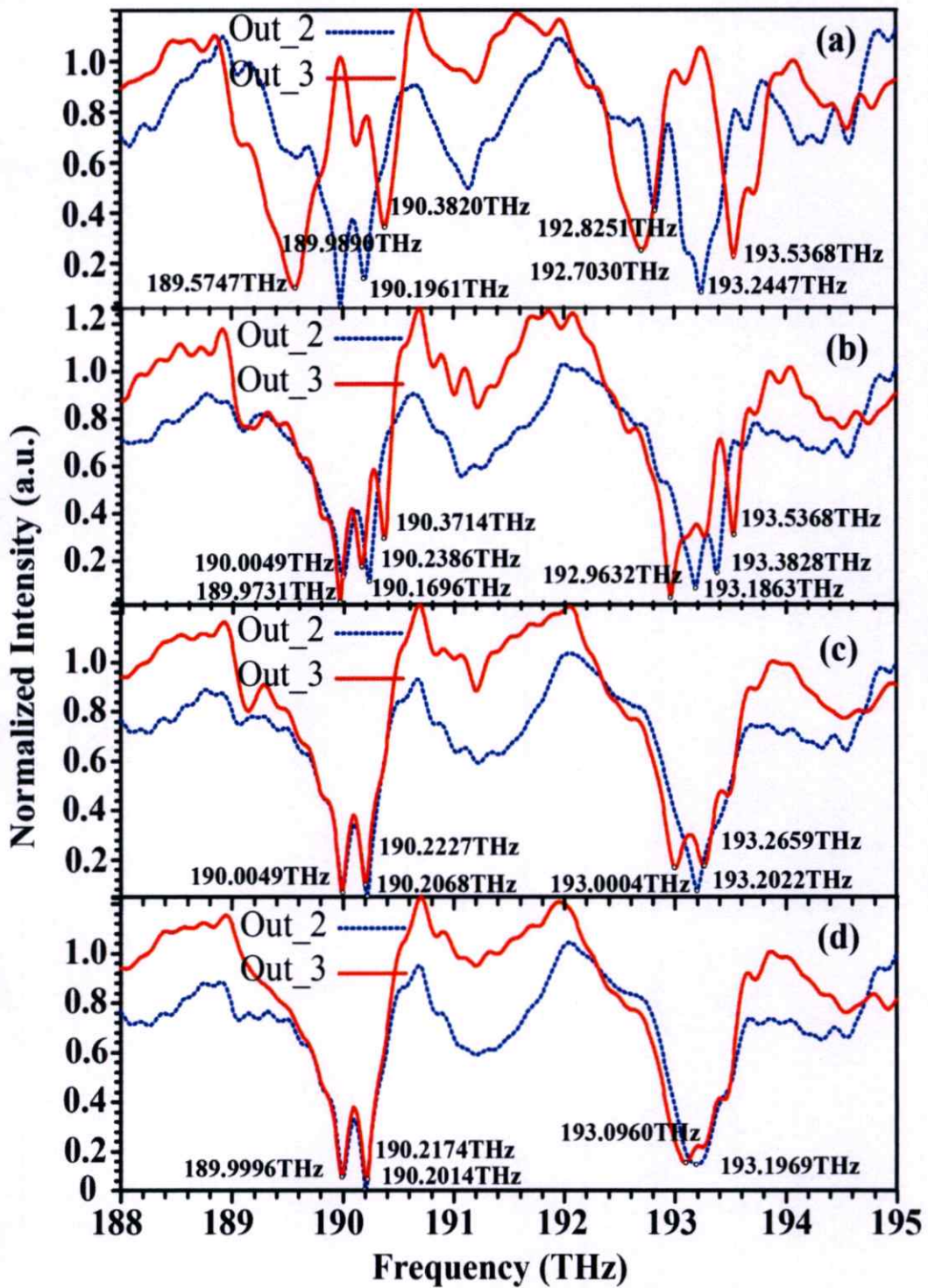


Figure. 4.16 The transmit (output) intensities are detect at the first, and second nested-microring resonator with gratings for varying gap coupling of the second nested-microring resonator, (a) $g = 0$, (b) $g = 100\text{nm}$, (c) $g = 200\text{nm}$, and (d) $g = 400\text{nm}$.

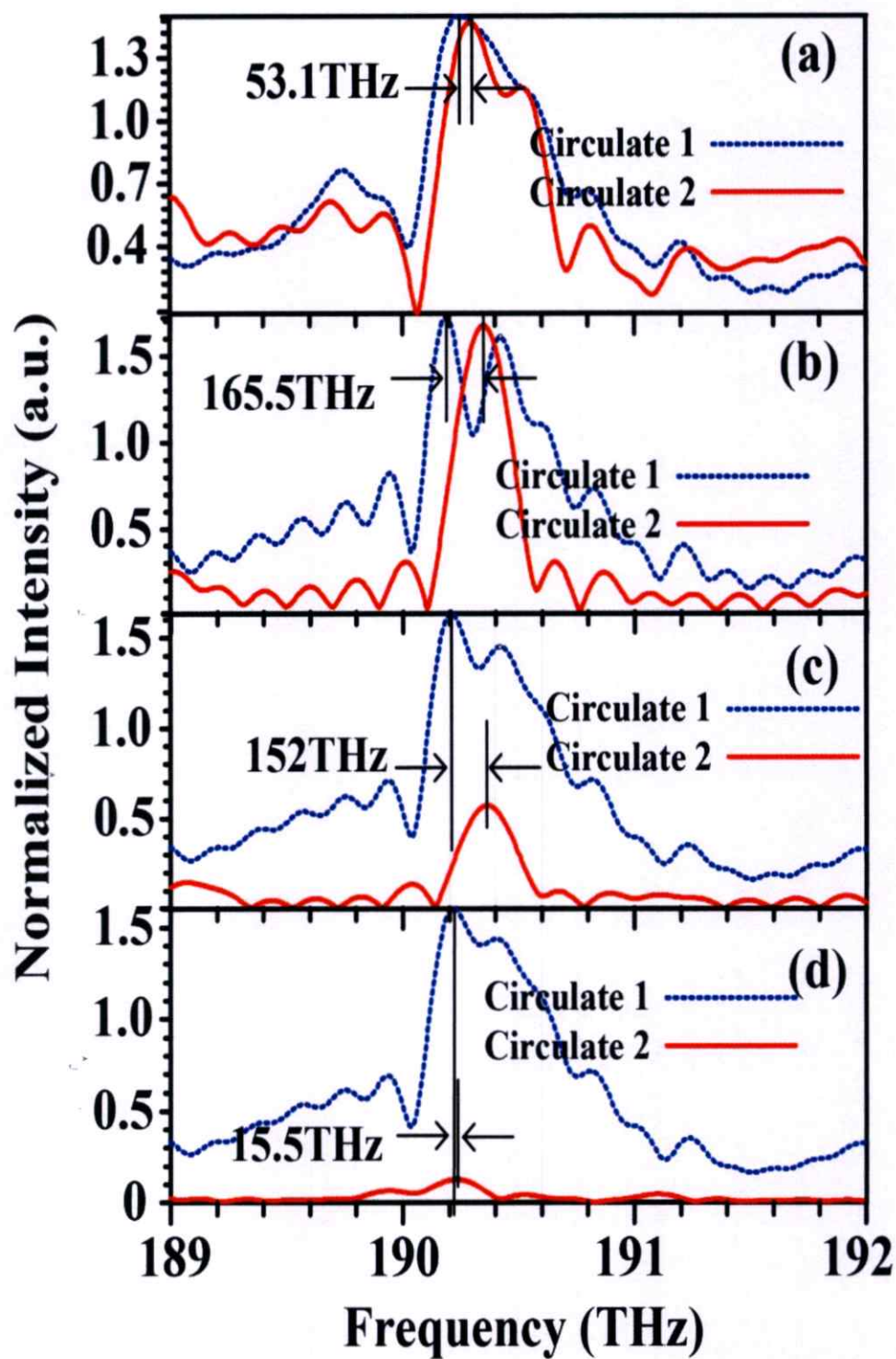


Figure. 4.17 The circulate intensity passes through the second nested-microring resonator with gratings for varies gap coupling (a) $g = 0$, (b) $g = 100$ nm, (c) $g = 200$ nm, and (d) $g = 400$ nm.

4.2.4 Vary Width of Waveguide and Nested Microring Resonators with gratings

In this section I fixed the waveguide high to be $0.5\mu\text{m}$. The width of the nested-microring (w_1) is varied from $0.3\mu\text{m}$ to $0.5\mu\text{m}$ and the bus waveguide (w_2) is varied from $0.5\mu\text{m}$ to $1.0\mu\text{m}$. For the $w_1 = 0.3\mu\text{m}$. The radii of nested-microring are $2.2, 2.5, 2.8, 3.1, 3.4, 3.7,$ and $4.0\mu\text{m}$, respectively, and the $w_2 = 0.5\mu\text{m}$, the radii of nested-microring are $1.0, 1.5, 2.0, 2.5, 3.0, 3.5,$ and $4.0\mu\text{m}$, respectively.

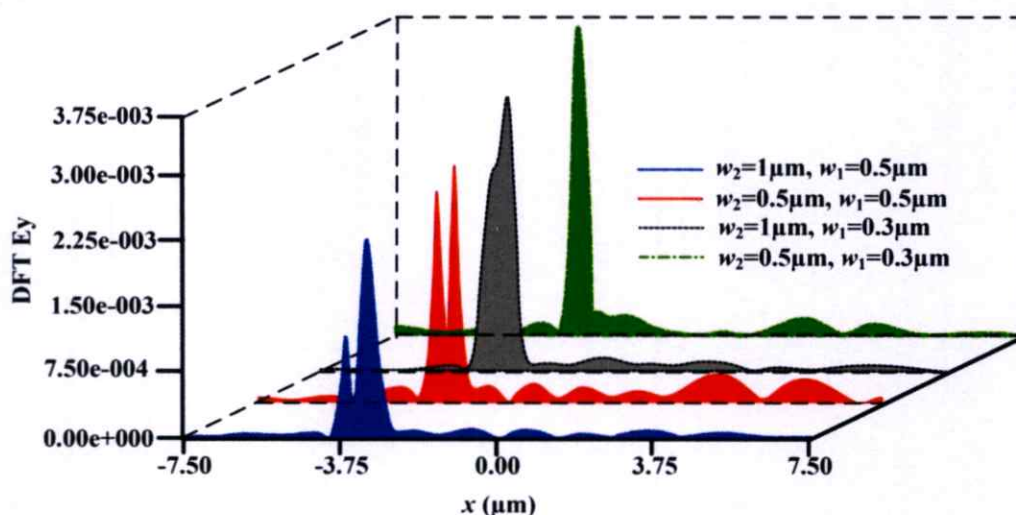


Figure. 4.18 The discrete flourier transform (DFT) of electric fields in y -direction for four optical waveguides design for vary the bus waveguide and nested MRR widths.

Figure. 4.18 shows the discrete flourier transform (DFT) of electric fields in y -direction for varying the widths of bus waveguide and nested-microring. I found that the electric fields resonant is spitted out to two peaks for the nested-microring width, w_1 , equal to $0.5\mu\text{m}$. The electric fields resonant is coupled into at once for the nested-microring width, w_1 , equal to $0.3\mu\text{m}$.

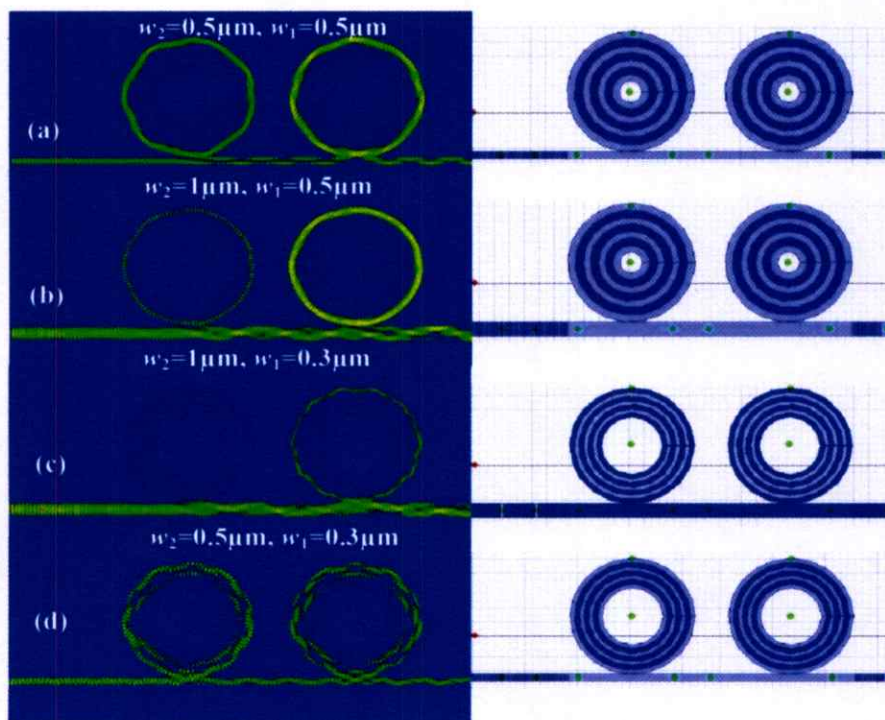


Figure. 4.19 The profile of light propagation in optical waveguides, (a) $w_1 = 0.5\mu\text{m}$, $w_2 = 0.5\mu\text{m}$, (b) $w_1 = 0.5\mu\text{m}$, $w_2 = 1.0\mu\text{m}$, (c) $w_1 = 0.3\mu\text{m}$, $w_2 = 1.0\mu\text{m}$, and (d) $w_1 = 0.3\mu\text{m}$, $w_2 = 0.5\mu\text{m}$.

Figure. 4.19 shows the profile of light intensity propagation in optical waveguides for Doppler frequency shift velocimeter application. I found that the light intensity is scattered in the bus width given to $1.0\mu\text{m}$ more than $0.5\mu\text{m}$. The resonant is occurred at the outer radii $4.0\mu\text{m}$ of nested-microring for width equal to $0.5\mu\text{m}$ (inner radii $1.0\mu\text{m}$). The light intensity is scattered at the multilayer of nested-microring for width equal to $0.3\mu\text{m}$ (inner and outer radii are $2.2\mu\text{m}$ and $4.0\mu\text{m}$, respectively).

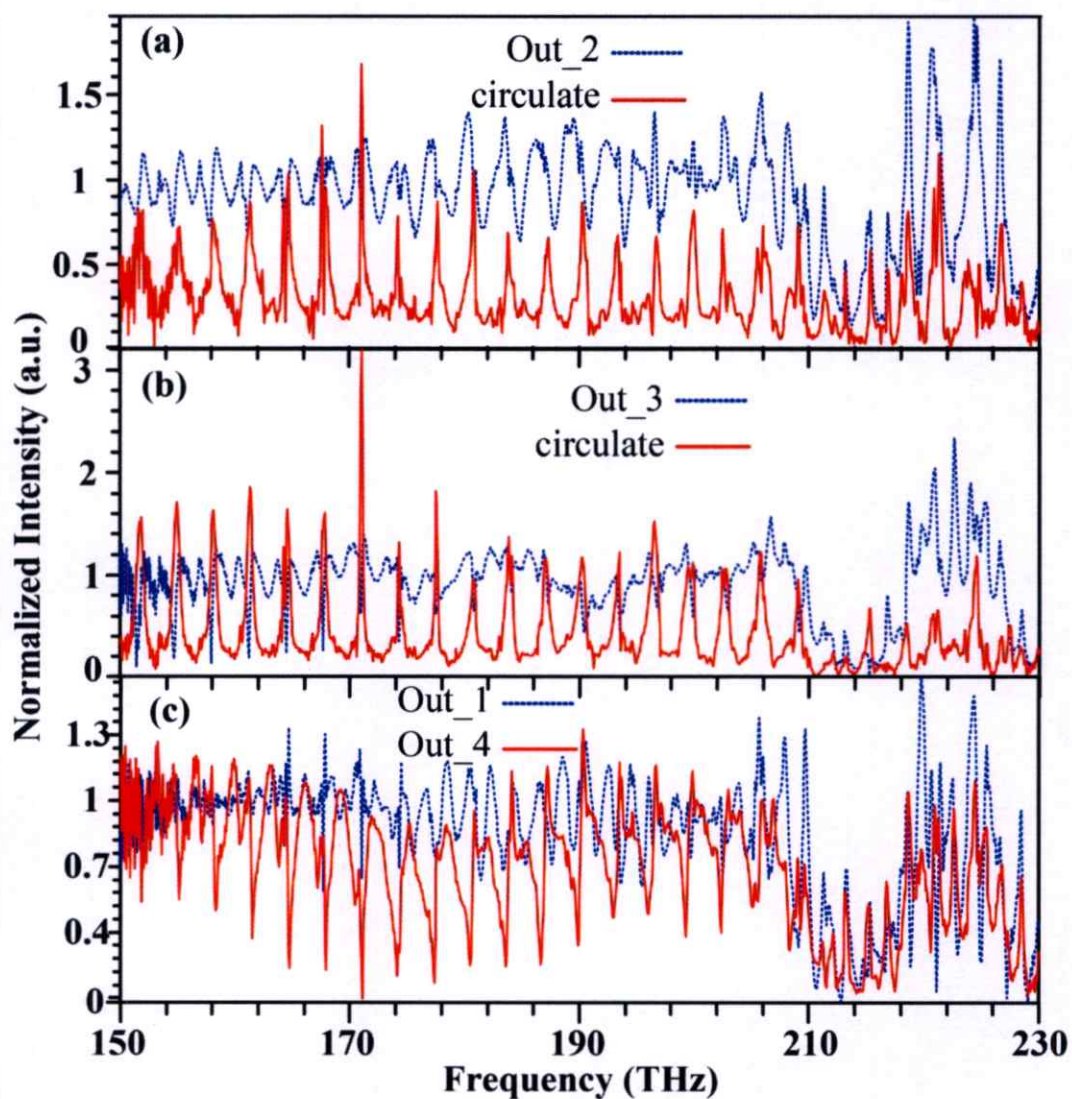


Figure. 4.20 The transmit (output) intensity for the bus waveguide width $w_2 = 1.0\mu\text{m}$ and the nested-microring width $w_1 = 0.5\mu\text{m}$.

Figure. 4.20 shows the transmission and circulation intensity as a function of the frequency for bus waveguide width $w_2 = 1.0\mu\text{m}$ and nested-microring width $w_1 = 0.5\mu\text{m}$. The “Reference” signal is shown in Figure. 4.20 (a) and the “Sensing” signal is shown in Figure. 4.20 (b), respectively.

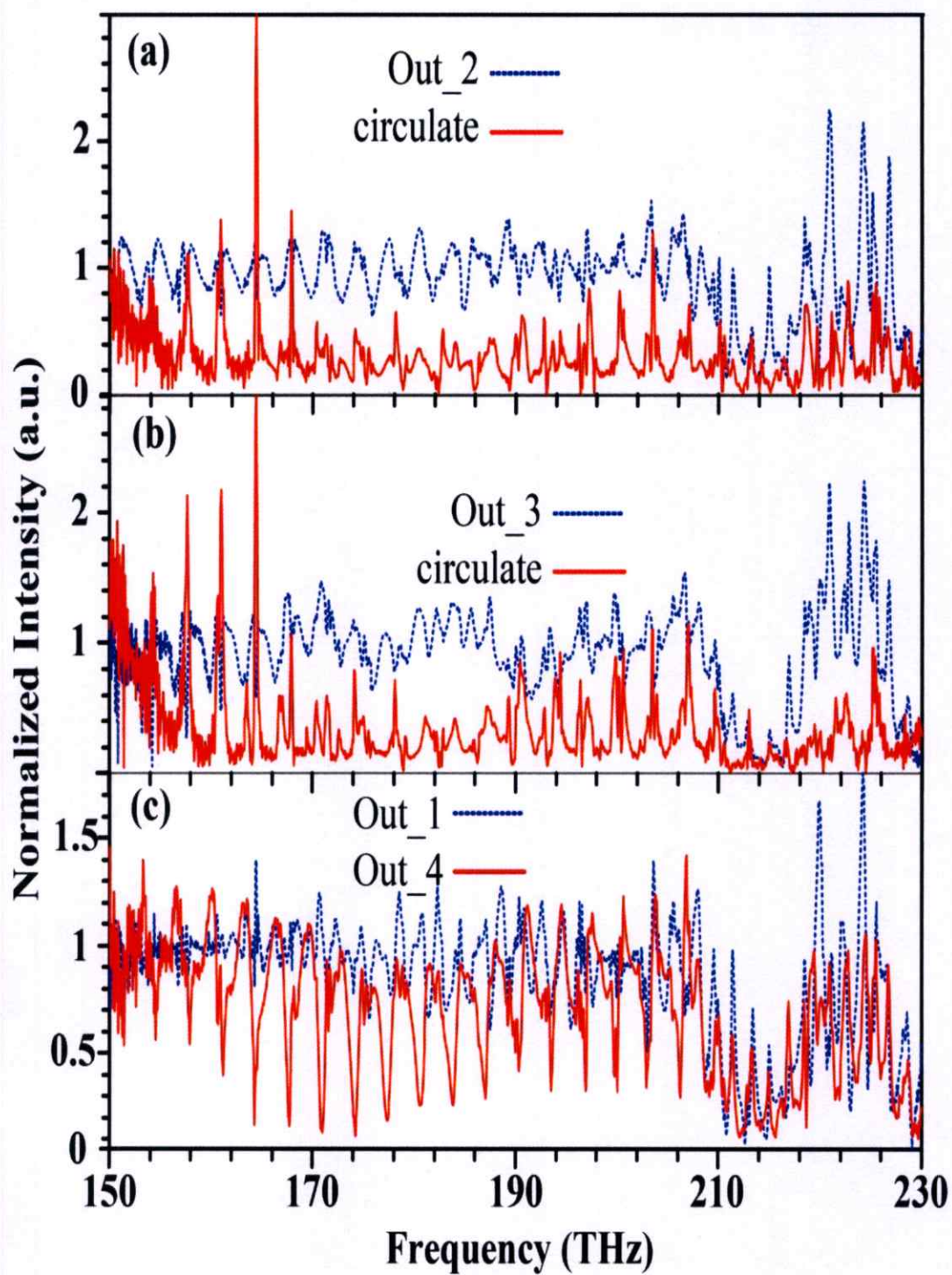


Figure. 4.21 The transmit (output) intensity for the bus waveguide width $w_2 = 1.0\mu\text{m}$ and the nested-microring width $w_1 = 0.3\mu\text{m}$.

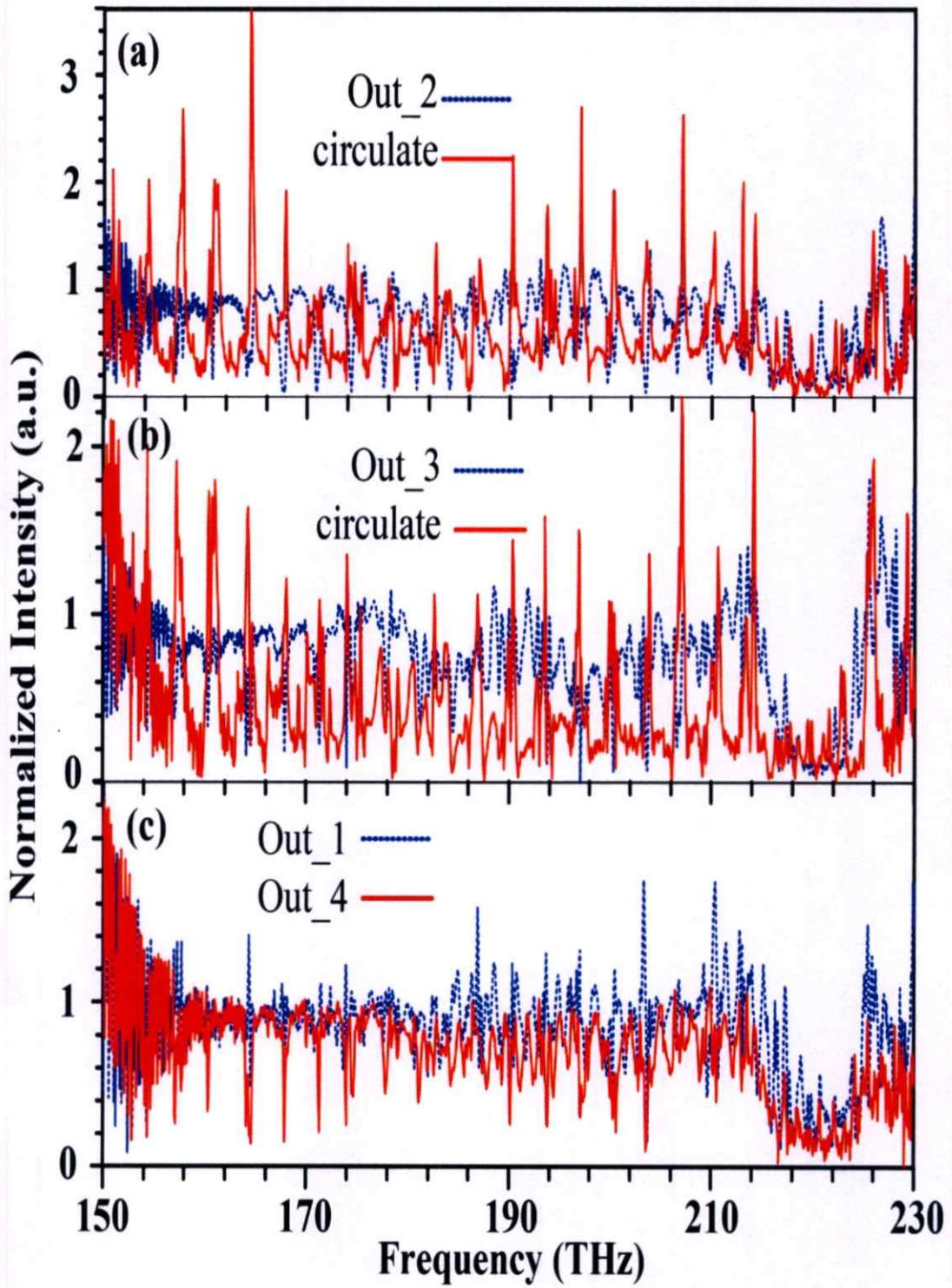


Figure. 4.22 The transmit (output) intensity for the bus waveguide width $w_2 = 0.5\mu\text{m}$ and the nested-microring width $w_1 = 0.3\mu\text{m}$.

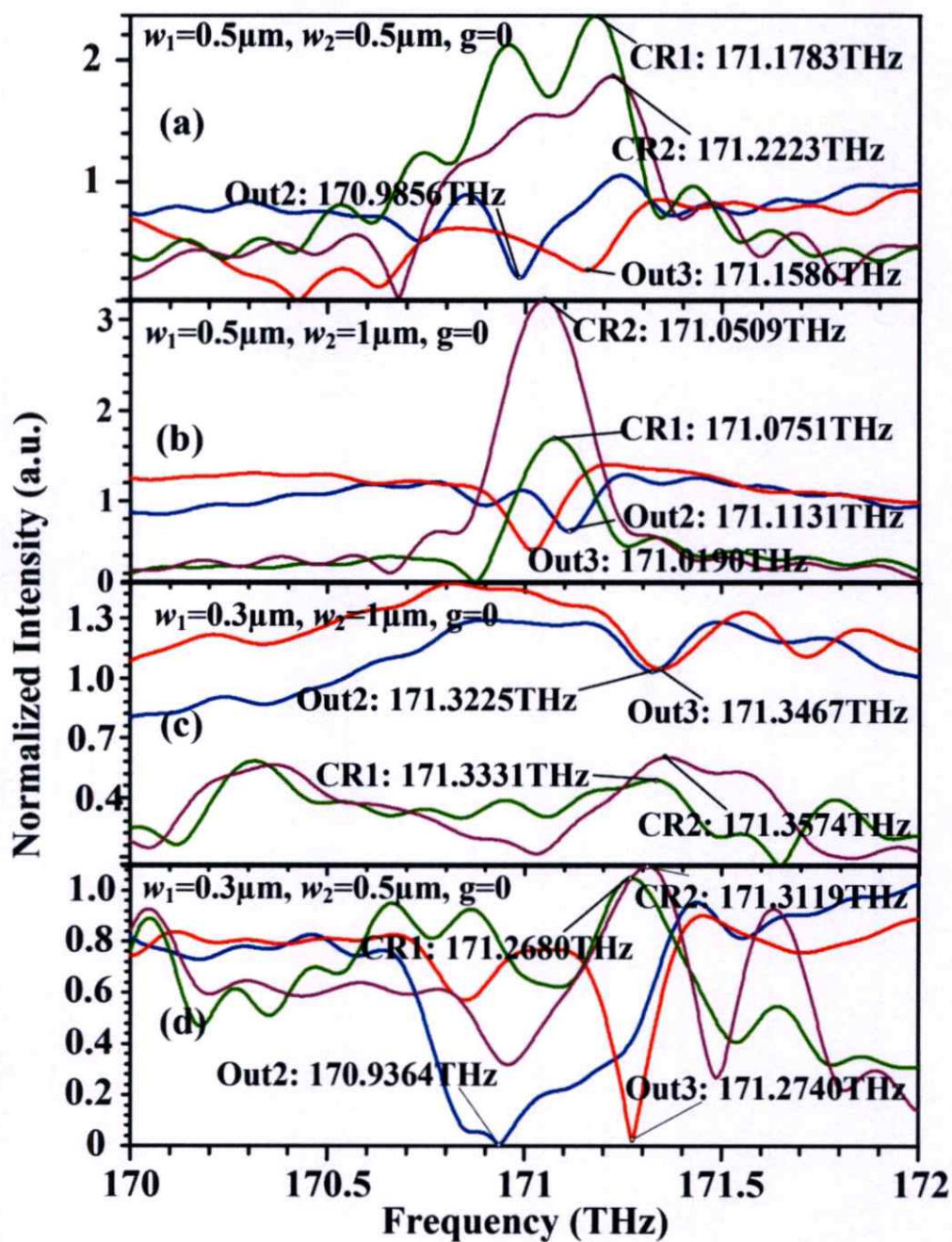


Figure. 4.23 The transmission (output) and circulation intensities for varying the width of nested-microring (w_1) and bus waveguide (w_2) in frequency range 170 – 172THz.

Figure. 4.23 shows the transmission (output) and circulation intensities for varying the width of nested-microring (w_1) and bus waveguide (w_2) in frequency range 170 – 172THz was investigated.

The relative velocity of transmission (output) intensity in the Figure. 4.23 (a) for the width of nested-microring ($w_1 = 0.5\mu\text{m}$) and bus waveguide ($w_2 = 0.5\mu\text{m}$) are 1.34×10^5 m/s (173GHz) and the relative velocity of circulation intensity is 3.41×10^4 m/s (44GHz).

The relative velocity of transmission (output) intensity in the Figure 4.23 (b) for the width of nested-microring ($w_1 = 0.5\mu\text{m}$) and bus waveguide ($w_2 = 1.0\mu\text{m}$) is 7.29×10^4 m/s (94.1GHz) and the relative velocity of circulation intensity is 1.88×10^4 m/s (24.2GHz).

The relative velocity of transmission (output) intensity in the Figure 4.23 (c) for the width of nested-microring ($w_1 = 0.3\mu\text{m}$) and bus waveguide ($w_2 = 1.0\mu\text{m}$) is 1.88×10^4 m/s (24.2GHz) and the relative velocity of circulation intensity is 1.88×10^4 m/s (24.3GHz).

The relative velocity of transmission (output) intensity in the Figure 4.23 (d) for the width of nested-microring ($w_1 = 0.3\mu\text{m}$) and bus waveguide ($w_2 = 0.5\mu\text{m}$) is 2.62×10^5 m/s (337.6GHz) and the relative velocity of circulation intensity is 3.40×10^4 m/s (43.9GHz).

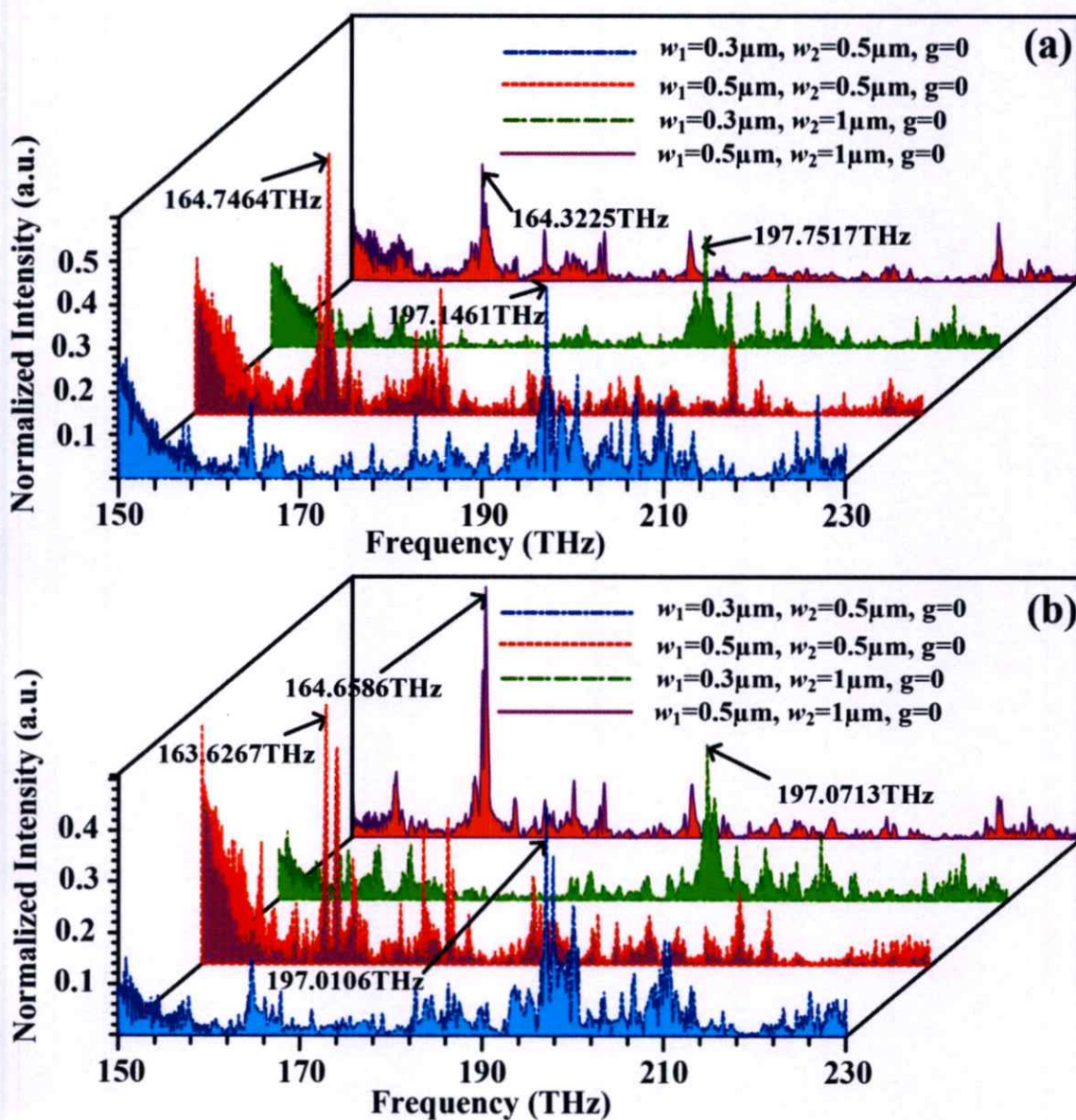


Figure. 4.24 The WGMs detect for vary the width of nested microring and bus waveguide for (a) first and (b) second of nested-microring resonators with gratings.

Figure. 4.24 shows the WGMs detecting for varying the width of nested microring and bus waveguide for (a) first and (b) second of nested-microring resonators with gratings. I found that the resonant intensity is occurred at the frequency about 197THz for the width of nested-microring equal to $0.3\mu\text{m}$ and the resonant intensity at the frequency about 164THz for the width of nested-microring

equal to $0.5\mu\text{m}$ both strong coupled mode ($g = 0$), respectively. The relative velocity for the width of nested-microring ($w_1 = 0.5\mu\text{m}$) and bus waveguide ($w_2 = 0.3\mu\text{m}$) is 1.05×10^5 m/s (135.5GHz). The relative velocity for the width of nested-microring ($w_1 = 0.5\mu\text{m}$) and bus waveguide ($w_2 = 0.5\mu\text{m}$) is 9.28×10^4 m/s (119.7GHz). The relative velocity for the width of nested-microring ($w_1 = 0.3\mu\text{m}$) and bus waveguide ($w_2 = 1.0\mu\text{m}$) are 5.27×10^5 m/s (680.4GHz). The relative velocity for the width of nested-microring ($w_1 = 0.5\mu\text{m}$) and bus waveguide ($w_2 = 1.0\mu\text{m}$) is 2.60×10^5 m/s (336.1GHz).

Chapter 5

Conclusions and Future Work

5.1 Transmission Characteristics of Optical Pulse in Nested Nonlinear Microring Resonators and Gratings

Nanoparticle grating modeling incorporating nested nonlinear microring resonator (NMR) and gratings are designed and simulated. The system model is consisted of two-defect grating, where the optical trapping tools are generated and launched into the waveguide of NMR and the uniform grating, in which the signal delay time is occurred and the transmission characteristics such as red-shifted, blue-shifted, trapping band can be seen. By using the input frequency center at 193.5THz, the blue-shifted is seen at the center frequency 215 THz, while the red-shifted is occurred at 175 THz. These can be used to form the optical tweezers for nanoparticle trapping. Moreover, the trapping particle Čerenkov radiation can also be investigated, which is useful for various applications, for instance, the transmission behaviors of output light can be used for application such as trapping tool, optical sensors and Čerenkov effects study [25–27].

By using the fast Fourier transform (FFT), the transmission spectrum of red-shifted Čerenkov radiations can be confirmed by the transmission behaviors of light pulse passing through the two-defect points of two-defect grating as shown in Fig. 8, where the red-shifted Čerenkov radiation has been studied in optical fiber by propagating light in LP02 mode [22, 26], which can be generated the red-shifted Čerenkov radiation, but in this model both red-shifted and blue-shifted Čerenkov radiations can be generated and seen.

5.2 Doppler Frequency Shift Velocimeter

I have shown the first Doppler frequency shift velocimeter by using the frequency shift of gratings coupled to the nested-microring resonators for velocity measurement. The frequency shift is generated by the path length interference between the transmission and circulation intensity of two nested-microring resonators. The relative velocity of Doppler frequency shift velocimeter has been measured frequency shift between the transmission and circulation intensity of two interfering nested-microring resonators.

In application, the Doppler frequency shift velocimeter can be used to measure the fluid flow [24], sensor probe [24, 25] etc.

5.3 Future Work

One of the main goals in this work was to observe optical phenomena in nested microring resonator. Even though I have reached many of targets, there is still scope for improvements and further exploration of some of the issues, such as

1. The sensors array generated by increasing the number of nested microring resonator.
2. The multi electron-hole pair based on optical phenomena.
3. The properties effect of optoelectronics spin-up and spin-down based on optical phenomena.

REFERENCES

1. A. Ashkin and J. M. Dziedzic, "Optical trapping and manipulation of viruses and bacteria," *Science* **235**(4795), 1517–1520 (1987).
2. H. Cai and A. W. Poon, "Optical trapping of microparticles using silicon nitride waveguide junctions and tapered-waveguide junctions on an optofluidic chip," *Lab Chip* **12**, 3803–3809 (2012).
3. H. Cai and A. W. Poon, "Optical manipulation and transport of microparticles on silicon nitride microring-resonator-based add-drop devices," *Opt. Lett.* **35**(17), 2855–2857 (2010).
4. N. Suwanpayak, M. A. Jalil, C. Teeka, J. Ali, and P. P. Yupapin, "Optical vortices generated by a PANDA ring resonator for drug trapping and delivery applications," *Biomed. Opt. Express* **2**(1), 159–168 (2011).
5. J. Lee, J. A. Grover, L. A. Orozco, and S. L. Rolston, "Sub-Doppler cooling of neutral atoms in a grating magneto-optical trap," *J. Opt. Soc. Am. B* **30**, 2869–2874 (2013).
6. H. Shen, G. Lu, T. Zhang, J. Liu, Y. He, Y. Wang, and Q. Gong, "Molecule fluorescence modified by a slit-based nanoantenna with dual gratings," *J. Opt. Soc. Am. B* **30**, 2420–2426 (2013).
7. J. Sakai and Y. Suzuki. "Equivalence between in-phase and antiresonant reflection conditions in Bragg fiber and its application to antiresonant reflecting optical waveguide-type fibers," *J. Opt. Soc. Am. B* **28**(1), 183-192 (2011).
8. P. Li and E. T. Yu, "Large-area omnidirectional antireflection coating on low-index materials," *J. Opt. Soc. Am. B* **30**, 2584–2588 (2013).
9. C. Vazquez and O. Schwelb. "Tunable, narrow-band, grating-assisted microring reflectors," *Opt. Comm.* **281**, 4910–4916 (2008).
10. I. Chremmos and O. Schwelb, "Optimization, bandwidth and the effect of loss on the characteristics of the coupled ring reflector," *Opt. Comm.* **282**, 3712–3719 (2009).

11. S.V. Pham, M. Dijkstra, A.J.F. Hollink, L.J. Kauppinen, R.M. de Ridder, M. Pollnau, P.V. Lambeck, and H.J.W.M. Hoekstra, "On-chip bulk-index concentration and direct, label-free protein sensing utilizing an optical grating-waveguide cavity," *Sens. Act. B: Chem.* **174**, 602–608 (2012).
12. Y. Lu, C. Hao, B. Lu, X. Huang, B. Wu, and J. Yao, "Transmission and group delay in a double microring resonator reflector," *Opt. Comm.* **285**, 4567–4570 (2012).
13. Y.M. Kang, A. Arbabi, and L. L. Goddard, "A microring resonator with an integrated Bragg grating: a compact replacement for a sampled grating distributed Bragg reflector," *Opt. Quant. Electron.* **41**, 689–697 (2009).
14. L.G. Yang, C.H. Yeh, C.Y. Wong, C.W. Chow, F.G. Tseng, and H.K. Tsang, "Stable and wavelength-tunable silicon-microring-resonator based erbium-doped fiber laser," *Opt. Express* **21**(3), 2869–2874 (2013).
15. X. Li, K. Xie, and H. -M. Jiang, "Properties of defect modes in one-dimensional photonic crystals containing two nonlinear defects," *Opt. Comm.* **282**, 4292–4295 (2009).
16. B. Lamprecht, G. Schider, R.T. Lechner, H. Ditlbacher, J.R. Krenn, A. Leitner, and F.R. Aussenegg, "Metal nanoparticle grating: Influence of dipolar particle interaction on the plasmon resonance," *Phys. Rev. Lett.* **84**(20), 4721–4724 (2000).
17. C. R. Philips, J. S. Pelc, and M. M. Fejer, "Parametric processes in quasi-phase matching gratings with random duty cycle errors," *J. Opt. Soc. Am. B* **30**, 982–993 (2013).
18. S.V. Zhukovsky, L. G. Helt, D. Kang, P. Abolghasem, A. S. Helmy, and J. E. Sipe, "Analytical description of photonic waveguides with multilayer claddings: towards on-chip generation of entangled photons and Bell states," *Opt. Comm.* **301–302**, 127–140 (2013).
19. C. Luo, M. Ibanescu, S. G. Johnson, and J. D. Joannopoulos, "Čerenkov radiation in photonic crystals," *Science* **299**, 368–371 (2003).
20. J. J. Saarinen and J. E. Sipe, "A Green function approach to surface optics in anisotropic media," *J. Mod. Opt.* **55**(1), 13–32 (2008).

21. G. L. Du, G. Q. Li, S. Z. Zhao, T. Li, and X. Li, "Theoretical analysis of electromagnetic field distribution and Cerenkov second harmonic generation conversion efficiency based on lithium niobate ion-implanted channel waveguide," *Optik* **123**, 896–900 (2012).
22. G. Du, G. Li, S. Zhao, X. Li, and Z. Yu, "Theoretical analysis of the TE mode Cerenkov type second harmonic generation in ion-implanted X-cut lithium niobate channel waveguides," *Opt. Laser Tech.* **44**, 830–838 (2012).
23. J. H. Lee, J. van Howe, C. Xu, and X. Liu, "Soliton self-frequency shift: experimental demonstrations and applications," *IEEE Select. Topics Quant. Electron.* **14**(3), 713–723 (2008).
24. B. Lastdrager, A. Tip, and J. Verhoeven, "Theory of Čerenkov and transition radiation from layered structures," *Phys. Rev. E* **61**, 5767–5778 (2000).
25. K. Kalinowski, V. Roppo, T. Lukasiwicz, M. Swirkowicz, Y. Sheng, and W. Krolikowski, "Parametric wave interaction in one-dimensional nonlinear photonic crystal with randomized distribution of second-order nonlinearity," *Appl. Phys. B* **109**, 557–566 (2012).
26. J. Cheng, J. H. Lee, K. Wang, C. Xu, K. G. Jespersen, M. Garmund, L. Grüner-Nielsen, and D. Jakobsen, "Generation of Cerenkov radiation at 850 nm in higher-order-mode fiber," *Opt. Express* **19**(9), 8774–8780 (2011).
27. B. Lee, K.W. Jang, W.J. Yoo, S.H. Shin, J. Moon, K. -T. Han, D. Jeon, "Measurements of Cerenkov lights using optical fibers," *IEEE Trans. Nucl. Sc.* **60**, 932–936 (2013).
28. X. Renzhen, L. Yuzheng, S. Zhimin, C. Changhua, and L. Guozhi, "Theoretical study of a plasma-filled relativistic Cerenkov generator with coaxial slow-wave structure," *IEEE Trans. Plasma Sc.* **35**(5), 145–1466 (2007).
29. S. A. Dekker, A. C. Judge, R. Pant, I. Gris-Sánchez, J. C. Knight, C. M. de Sterke, and B. J. Eggleton, "Highly-efficient, octave spanning soliton self-frequency shift using a specialized photonic crystal fiber with low OH loss," *Opt. Express* **19**(18), 17766–17773 (2011).
30. W. Wang, Y. Sheng, X. Niu, M. Huang, S. Zheng, and Y. Kong, "Second harmonic Cerenkov radiation in bulk birefringent quadratic medium without any $\chi^{(2)}$ modulation," *Opt. Laser Techn.*, **58**, 16–19 (2014).
31. H. Chen and M. Chen, "Flipping photons backward; reversed Cherenkov radiation," *Mater. Today*, **14**(1-2), 34–41 (2011).

32. W. J. Yoo, S. H. Shin, D. Jeon, S. Hong, S. G. Kim, H. I. Sim, K. W. Jang, S. Cho, and B. Lee, "Simultaneous measurements of pure scintillation and Cerenkov signals in an integrated fiber-optic dosimeter for electron beam therapy dosimetry," *Opt. Express* **21**(23), 27770–27779 (2013).
33. K. W. Jang, W. J. Yoo, S. H. Shin, D. Shin, and B. Lee, "Fiber-optic Cerenkov radiation sensor for proton therapy dosimetry," *Opt. Express* **20**(13), 13907–13914 (2012).
34. S. Li, K. Kang, Y. Wang, J. Li, J.-J. Song, and Y. Li, "Using a Cerenkov detector in HVL measurements for industrial electron linacs," *Rad. Measur.*, **46**, 726–729 (2011).
35. C. Qin, J. Zhong, Z. Hu, X. Yang, and J. Tian, "Recent advances in Cerenkov luminescence and tomography imaging," *IEEE Select. Topics Quant. Electron.* **18**(3), 1084–1093 (2012).
36. I. Silva and G. Pang, "Characteristics of radiation induced light in optical fibres for portal imaging application," *Rad. Phys. Chem.* **81**, 599–608 (2012).
37. K. W. Jang, T. Yagi, C. H. Pyeon, W. J. Yoo, S. H. Shin, T. Misawa, and B. Lee, "Feasibility of fiber-optic radiation sensor using Cerenkov effect for detecting thermal neutrons," *Opt. Express* **21**(12), 14573–14582 (2013).
38. R. Jomtarak and P. P. Yupapin, "Transmission characteristics of optical pulse in nested nonlinear microring resonators and gratings," *J. Opt. Soc. Am. B*, **31**, 474 – 477, 2014.
39. K. Maru and Y. Fujii, "Wavelength-insensitive laser Doppler velocimeter using beam position shift induced by Mach-Zehnder interferometers," *Opt. Express*, **17**(20), 17441 – 17449, 2009.
40. K. Maru and Y. Fujii, "Differential laser Doppler velocimeter with enhanced range for small wavelength sensitivity by using cascaded Mach-Zehnder interferometers," *J. Lightw. Technol.*, **28**(11), 1631 – 1637, 2010.
41. K. Maru and Y. Fujii, "Laser Doppler velocimetry for two-dimensional directional discrimination by monitoring scattered beams in different directions," *IEEE Sensors*, **11**(2), 312 – 318, 2011.
42. K. Maru, L. Y. Hu, R. S. Lu, Y. Fujii, and P. P. Yupapin, "Two-dimensional laser Doppler velocimeter using polarized beams and 90° phase shift for discrimination of velocity direction," *Optik*, **122**, 974 – 977, 2011.
43. K. Maru and K. Watanabe, "Non-mechanical scanning laser Doppler velocimetry with sensitivity to direction of transverse velocity component using optical serrodyne frequency shifting," *Opt. Comm.*, **319**, 80 – 84, 2014.

44. K. Maru and K. Fujimoto, "Demonstration of two-point velocity measurement using diffraction grating elements for integrated multi-point differential laser Doppler velocimeter," *Optik*, **125**, 1625 – 1628, 2014.
45. K. Maru, K. Kobayashi, and Y. Fujii, "Multi-point differential laser Doppler velocimeter using arrayed waveguide gratings with small wavelength sensitivity," *Opt. Express*, **18**(1), 301 – 308, 2009.
46. F. Li, H. Murayama, K. Kageyama, and T. Shirai, "Doppler effect-based fiber-optic sensor and its application in ultrasonic detection," *Opt. Fiber Technol.*, **15**, 296 – 303, 2009.
47. P. J. Rodrigo and C. Pedersen, "Monostatic coaxial 1.5 μ m laser Doppler velocimeter using a scanning Fabry-Perot interferometer," *Opt. Express*, **21**(18), 21105 – 21112, 2013.
48. J. Walther and E. Koch, "Transverse motion as a source of noise and reduced correlation of the Doppler phase shift in spectral domain OCT," *Opt. Express*, **17**(22), 19698 – 19713, 2009.
49. B. Varghese, V. Rajan, T. G. van Leeuwen, and W. Steenbergen, "Discrimination between Doppler-shifted and non-shifted light in coherence domain path length resolved measurements of multiply scattered light," *Opt. Express*, **15**(20), 13340 – 13350, 2007.
50. B. Varghese, V. Rajan, T. G. van Leeuwen, and W. Steenbergen, "Measurement of particle flux in a static matrix with suppressed influence of optical properties, using low coherence interferometry," *Opt. Express*, **18**(3), 2849 – 2857, 2010.
51. Y. Bai, D. Ren, W. Zhao, Y. Qu, L. Qian, and Z. Chen, "Heterodyne Doppler velocity measurement of moving targets by mode-locked pulse laser," *Opt. Express*, **20**(2), 764 – 768, 2012.
52. M. C. Hirschberger and G. Ehret, "Simulation and high-precision wavelength determination of noisy 2D Fabry-Perot interferometric rings for direct-detection Doppler lidar and laser spectroscopy," *Appl. Phys. B*, **103**, 207 – 222, 2011.
53. L. Keruevan, H. Gilles, S. Girard, M. Laroche, and P. Leprince, "Self-mixing laser Doppler velocimetry with a dual-polarization Yb:Er glass laser," *Appl. Phys. B*, **86**, 169 – 176, 2007.
54. Dan T. Nguyen and Robert A. Norwood. Label-free, single-object sensing with a microring resonator: FDTD simulation. *Opt. Express* **21**(2013)49-59.

55. A. M. Armani, R. P. Kulkarni, S. E. Fraser, R. C. Flagan, and K. J. Vahala, "Label-free, single-molecule detection with optical microcavities," *Science* **317**(5839), 783–787 (2007).
56. F. Vollmer, D. Braun, A. Libchaber, M. Khoshima, I. Teraoka, and S. Arnold, "Protein detection by optical shift of a resonant microcavity," *Appl. Phys. Lett.* **80**(21), 4057–4059 (2002).
57. F. Vollmer and S. Arnold, "Whispering-gallery-mode biosensing: label-free detection down to single molecules," *Nat. Methods* **5**(7), 591–596 (2008).
58. X. Chen, C. Li, C. K. Y. Fung, S. M. G. Lo, and H. K. Tsang, "Apodized Waveguide Grating Couplers for Efficient Coupling to Optical Fibers," *IEEE Photon. Technol. Lett.* **22**(15), 1156–1158 (2010).
59. D. Taillaert, F. Van Laere, M. Ayre, W. Bogaerts, D. Van Thourhout, P. Bienstman, and R. Baets, "Grating couplers for coupling between optical fibers and nanophotonic waveguides," *Jpn. J. Appl. Phys.* **45**(8A), 6071–6077 (2006).
60. B. Liu, A. Shakouri, and J. E. Bowers, "Passive microring-resonator-coupled lasers," *Appl. Phys. Lett.* **79**(22), 3561–3563 (2001).
61. K. Maru, "Axial scanning laser Doppler velocimeter using wavelength change without moving mechanism in sensor probe," *Opt. Express*, **19**(7), 5960 – 5969, 2011.
62. P. Kaspar, R. Kappeler, D. Erni, and H. Jackel, "Average light velocities in periodic media," *J. Opt. Soc. Am. B* **30**, 2849–2854 (2013).
63. M. Cheng, "Forward-and backward-propagating Cerenkov radiation in strong chiral media," *Opt. Express*, **15**(15), 9793–9798 (2007).
64. J. Arlt, M. MacDonald, L. Paterson, W. Sibbett, and K. Dholakia, "Moving interference patterns created using the angular Doppler-effect," *Opt. Express*, **10**(16), 844 – 852, 2002.
65. G. Morthier and P. Mechet, "Theoretical analysis of unidirectional operation and reflection sensitivity of semiconductor ring or disk lasers," *IEEE Quan. Electron.*, **49**(12), 1097 – 1101, 2013.
66. G. C. Righini, Y. Dumeige, P. Féron, M. Ferrari, G. Nunzi Conti, D. Ristic, and S. Soria, "Whispering gallery mode microresonators: Fundamentals and applications," *RIVISTA DEL NUOVO CIMENTO*, **34**(7), 435 - 488, 2011.

67. D. O'Shea, C. Junge, M. Pöllinger, A. Vogler, and A. Rauschenbeutel, "All-optical switching and strong coupling using tunable whispering gallery mode microresonators," *Appl. Phys. B*, **105**, 129 – 148, 2011.
69. F. Monifi, J. Friedlein, S. K. Özdemir, and L. Yang, "A robust and tunable add-drop filter using whispering gallery mode microtoroid resonator," *J. Lightw. Technol.*, **30**(21), 3306 – 3315, 2012.
70. F. de Leonardis and V. M. N. Passaro, "Scattering effect in optical microring resonators," *J. Comput. Electron.*, **6**, 293 – 296, 2007.
71. Y. Liu, T. Chang, and A. E. Craig, "Coupled mode theory for modeling microring resonators," *Opt. Eng.*, **44**(8), 084601, August 2005.
72. S. Sudo, Y. Miyasaka, K. Nemoto, K. Kamikariya, and K. Otsuka, "Detection of small particles in fluid flow using a self-mixing laser," *Opt. Express*, **15**(13), 8135 – 8145, 2007.
73. P. Günther, T. Pfister, L. Büttner, and J. Czarske, "Laser Doppler distance sensor using phase evaluation," *Opt Express*, **17**(4), 2611 – 2622, 2009.
74. W. Chao, C.Y. and Fung and L.J. Guo. Polymer microring resonators for biochemical sensing applications. *Selected Topics in Quantum Electronics, IEEE Journal of*, **12**(1):134–142, 2006.

Biography

Name	Mr. Rangsan Jomtarak
Date of Birth	30 December 1979
Address	Department of Physics, Faculty of Science and Technology, Suan Dusit University, Bangkok 10700, Thailand.
Education	(2002) Bachelor's Degree in General science (Institute) Suan Dusit Rajabhat (2008) Master of Science in Applied Radiation and Isotopes (University) Kasetsart
Scholarship	Suan Dusit Rajabhat University

Academic Publications

1. R. Jomtarak and P. P. Yupapin, "Transmission characteristics of optical pulse in nested nonlinear microring resonators and gratings," *J. Opt. Soc. Am. B*, **31**, 474 – 477, 2014.
2. R. Jomtarak , P. P. Yupapin and J. Ali, "Doppler shift velocimetry using two point probe nested- microring resonators," *Journal of Nonlinear Optical Physics and Materials*, Vol. **24**, No. 1 1550003, 2015.